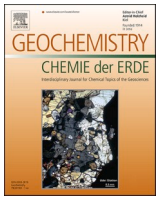
Geochemistry 85 (2025) 126303



Contents lists available at ScienceDirect

Geochemistry

journal homepage: www.elsevier.com/locate/chemer





Mixed fluid processes in Fe—Mn dendrite formation and associated carbon and nickel isotope fractionation

Anna Neubeck [a,*], Piotr Szymczak [b], Vyllinniskii Cameron [a], Daniel Buczko [a], Magnus Ivarsson [c]

[a] Department of Earth Sciences, Uppsala University, Sweden
[b] Institute of Theoretical physics, Faculty of physics, University of Warsaw, Poland
[c] Swedish Museum of Natural History, Stockholm, Sweden

ARTICLE INFO

Handling Editor: Federico Lucci

Keywords:
Fe—Mn dendrites
Carbon isotopes
Nickel isotopes
Mixed fluid formation
Subsurface
Ultramafic
Serpentinization

ABSTRACT

Dendritic iron- and/or manganese-rich microstructures, often referred to as "microstromatolites," are commonly observed in carbonate veins in the deep subsurface. However, the mechanisms responsible for their formation, particularly the role of microbial processes, remain incompletely understood. One hypothesis suggests that Fe- and Mn-enriched fluids, sourced from submarine hydrothermal vents and circulating through mafic or ultramafic rocks, lead to the precipitation of manganese dendrites within open fractures. Microbial activity has been proposed as a contributing factor, particularly due to its ability to catalyze Mn^{2+} oxidation to Mn^{4+} at rates significantly faster than abiotic processes under ambient conditions. Such microbial mediation often results in the formation of poorly crystalline Mn oxide phases, which are commonly associated with biologically mediated oxidation. These disordered Mn oxides, frequently observed in natural settings, suggest a microbial contribution to mineral precipitation, particularly in environments where redox gradients and fluid-rock interactions are prominent. Because manganese oxides are an important sink for Ni in marine systems, stable Ni isotope analyses may offer valuable insights into their formation. Biological activity in laboratory systems is known to fractionate Ni isotopes, producing negative δ^{60}Ni values, while abiotic interactions with Mn oxides can result in a range of isotopic signatures. In this study, we show that manganese-rich dendrites likely formed through the interplay between organic matter, oxidizing fluids and viscous serpentine muds, resulting in the fractionation of both carbon and nickel isotopes. The moderately negative δ^{13}C and δ^{60}Ni values, together with the presence of organic matter, suggest a mixed formation pathway involving both abiotic mineral precipitation and biologically mediated processes. One plausible mechanism involves the nucleation of Mn oxides on nanoparticulate "seeds," which could include both abiotic particles, organic matter, microbial cells and their metabolic byproducts. Understanding the formation of Fe—Mn dendrites is key to interpreting the biogeochemical cycling of essential elements like iron, manganese, and nickel. Due to its redox flexibility, Mn forms highly reactive oxides that effectively scavenge trace metals such as Ni, Co, Fe, and Cu, facilitating their removal from seawater and incorporation into marine minerals. Our findings underscore the complexity of Fe—Mn oxide formation and point to the combined influence of abiotic fluid dynamics and microbial processes. This improves our ability to interpret geochemical signatures in both modern and ancient environments and enhances the utility of stable isotope systems in reconstructing past ocean conditions and elemental cycling.

1. Introduction

Both Fe and/or Mn-rich, microbial dendritic microstromatolites and abiotic dendrites formed through viscosity differences can look remarkably similar, especially when viewed at small scales (Böhm and Brachert, 1993; Garcia-Ruiz et al., 1994; Heim et al., 2017; Hou et al., 2023; Kazmierczak and Kempe, 2006; Myrow and Coniglio, 1991; Saunders, 2022; Saunders and Schoenly, 1995; Schoenly and Saunders, 1993). While microbial stromatolites form as a result of biological processes, viscosity-driven dendrites result from non-biological fluid dynamics, yet, both can develop in similar settings despite entirely different mechanisms. Environments hosting three-dimensional dendrite structures can be very diverse. For instance, silica-rich fluids are commonly associated with abiotic dendrites (Hou et al., 2023;

* Corresponding author.
E-mail address: anna.neubeck@geo.uu.se (A. Neubeck).

https://doi.org/10.1016/j.chemer.2025.126303
Received 28 October 2024; Received in revised form 24 April 2025; Accepted 25 May 2025
Available online 28 May 2025
0009-2819/© 2025 The Author(s). Published by Elsevier GmbH. This is an open access article under the CC BY license (http://creativecommons.org/licenses/by/4.0/).

Kazmierczak and Kempe, 2006; Myrow and Coniglio, 1991; Saunders, 2022; Saunders and Schoenly, 1995; Schoenly and Saunders, 1993). On the other hand, most microstromatolitic Fe-Mn-dendrites found in carbonate rocks are considered biogenic (Cavalazzi et al., 2007; Eder et al., 2018; Zhang et al., 2021; Bernardini et al., 2021a, 2021b), including examples found in cherts (Walter and Awramik, 1979). Thus, both microbial stromatolites and abiotic, viscosity formed dendrites can occur in similar rock types and depositional settings, such as carbonates and silicates. The overlapping environmental contexts complicate distinguishing between the two, especially when examining fossilized samples where biological signatures of microbial life may be absent or poorly preserved. Isotopic methods, particularly involving C and S, have traditionally been used to differentiate biological from abiotic microstructures. Increasingly, researchers also use transition metal isotopes, with Ni emerging as a promising biomarker due to its role in some enzymes and its distribution in oceanic environments, reflecting paleoredox and paleoproductivity conditions (Cameron et al., 2009; Cameron and Vance, 2014; Ciscato et al., 2018; Lemaitre et al., 2022; Vance et al., 2016; Ragsdale, 2007, 2009). Nickel has a strong affinity for organic ligands and approximately 35 % of all marine dissolved Ni is bound to organic compounds. However, due to its electron configuration, [Ar] $4s^2 3d^8$, it has a higher Z_{eff} (effective nuclear charge) than for example Fe, which results in stronger bounded electrons, leading to slower complexation kinetics (Pyle and Couture, 2011). Also, O and N donor atoms, classified as hard bases, prefer to bind to hard acids like many transition metal ions (including Ni^{2+} and Fe^{2+}), through ionic interactions that are generally strong and straightforward. This leads to faster formation of complexes because the metal ions are highly attracted to these ligands and the energy barriers for complexation are lower. In contrast, many organic ligands are considered soft bases and tend to interact with transition metals through covalent bonding, often involving additional steps such as rearrangements or electron pair sharing. These interactions are typically complex and slower, leading to a reduced rate of complexation (Pearson, 1963). Nickel is more strongly bound to oxygen in mineral phases such as Fe—Mn nodules than to organic ligands. As a result, Ni associated with organic matter tends to exhibit more negative δ values compared to Ni sequestered in Fe—Mn nodules. Although organic matter can influence the speciation of Ni locally, especially in organic-rich sediments, its role in the global marine Ni budget appears limited. This is because the majority of Ni in such settings remains bound to mineral phases rather than to organic compounds, as observed in organic-rich marine sediments where the total Ni content is still largely controlled by Fe—Mn oxides (e.g., Gueguen and Rouxel, 2021). Consequently, the impact of organic-bound Ni on the overall marine Ni mass balance is likely minor. This is consistent with the interpretation that Fe—Mn nodules represent a primary long-term sink for Ni in the ocean. Among these phases, hydrous Mn oxides play a particularly important role in Ni retention due to their high metal adsorption capacity and greater stability across pH gradients compared to Fe oxides (Green-Pedersen et al., 1997; Pyle and Couture, 2011). The δ^{60}Ni values of marine Fe—Mn crusts analyzed range between +0.25 ‰ and + 2.5 ‰ (Gall et al., 2013; Gueguen et al., 2016), while most laboratory experiments have shown much lighter values, as low as −1.34 ‰ (Sorensen et al., 2020; Wasylenki et al., 2014, 2024). However, the main mineralogy of deeply buried marine ferromanganese nodules has by some researchers been shown to be todorokite, which is topotactically formed mainly from phyllomanganates (mainly birnessites) under oxic to suboxic conditions (Li et al., 2024). During the transformation from birnessite to todorokite, the isotopic signature of Ni would gradually become heavier. Other studies indicate a more complex mineralogy, primarily composed of poorly crystalline phyllomanganates, and suggest that redox transitions from formation to diagenesis in ferromanganese crusts are characterized by changes in oxidation states, mineralogy, post-depositional oxidation, and element associations, which can significantly influence the fractionation of associated isotopes (Sutherland et al., 2020; Xu et al., 2024). This temporal evolution of natural nodules would explain the experimental observations in which birnessites exhibit a preference for lighter Ni isotopes (Sorensen et al., 2020; Wasylenki et al., 2014, 2024), while naturally occurring Fe—Mn nodules display comparatively heavier Ni isotope compositions. Thus, light Ni may end up elsewhere during the nodule evolution, such as other Mn-rich, phyllomanganates not directly associated with Fe—Mn nodule formations. Examples of such associations are presented by Fleischmann et al. (2023), showing that fully oxic, Mn-rich pelagic sediments across six sites in the Pacific Ocean and ten in the Indian Ocean, as well as one hemipelagic site from the suboxic California Margin, have Ni isotope compositions (δ^{60}Ni = +0.26 to +1.08 ‰) lighter than seawater (+1.33 ‰) and crusts (+1.55 ± 0.38 ‰) and that the organic carbon-rich suboxic sediments of the Californian margin have even lighter values of δ^{60}Ni = −0.08 ± 0.11 ‰. This study examines Mn-, Fe- and organic-rich serpentine mud, which may show similar features as described by Fleischmann et al. (2023), associated with low-temperature (<100 °C) serpentinization from the Mid-Atlantic Ridge in an attempt to understand and distinguish between abiotically and biologically formed Fe—Mn dendrites (Alt et al., 2007). Microdrilled samples were analyzed by multi-collector inductively coupled plasma mass spectrometry (MC-ICP-MS) to assess the potential association of light Ni with Mn, distinct from Fe—Mn nodules. Carbon isotope analyses of Fe and/or Mn-rich microstromatolites are rare and range broadly between −35 ‰ to +1.7 ‰ (Andrews et al., 2015; Neubeck et al., 2021; Zwicker et al., 2023) and only one of these studies have reported abundant Mn (Neubeck et al., 2021). Thus, it is still unclear whether microstromatolitic and Mn-rich dendrites in the deep subsurface are mainly biogenic or if there are other processes that may influence the formation of such structures in igneous rock environments. Here we aim to add further insights into the formation process of such microstructures in a serpentinized, low-temperature marine environment, using stable isotopes of C and Ni.

2. Methodology

2.1. Sample description

The sample analyzed in this study is a thin section from Hole 1272 A, North Pond, recovered during Ocean Drilling Program (ODP) Leg 209 from the slow-spreading Mid-Atlantic Ridge (MAR) (Kelemen et al., 2004; Alt et al., 2007), see Fig. 1. Hole 1272 A, located at Site 1272 (approximately 15°39.9′N, 56°45.6′W), was drilled near the top of a ridge composed primarily of serpentinized peridotite, ~3.7 nautical miles north of Site 1271. Coring proceeded from Core 1R to Core 27R, reaching a total depth of 131.0 m below seafloor (mbsf). After reaching 131.0 mbsf with consistent lithology and drilling conditions, coring was halted and followed by successful wireline logging before the hole was terminated. The sample for this study was collected at 40–45 m below seafloor (mbsf), a depth characterized by multiple faults and diverse lithologies. The host rocks are serpentinized ultramafic harzburgites and dunites, altered to soft, clayey serpentine- and harzburgite-rich muds, which appeared plastic upon core recovery (Bach et al., 2004).

The section contains several small (mm-scale) and one large (1 cm-wide) aragonite vein cutting through serpentine clays. These veins exhibit reddish to brownish halos rich in iron hydroxides, indicative of precipitation from oxygenated seawater during late-stage exhumation and brittle faulting.

On the wall of the large vein, dendritic structures (a few hundred μm long, up to 50 μm wide) protrude perpendicularly into the surrounding serpentine and are partly embedded in aragonite (Fig. 2). Additional dendritic and filamentous structures are fully embedded in aragonite (Neubeck et al., 2021; Ivarsson et al., 2018). The dendrites observed in the serpentine muds appear dark to black in optical microscopy and show frequent branching (Fig. 2).

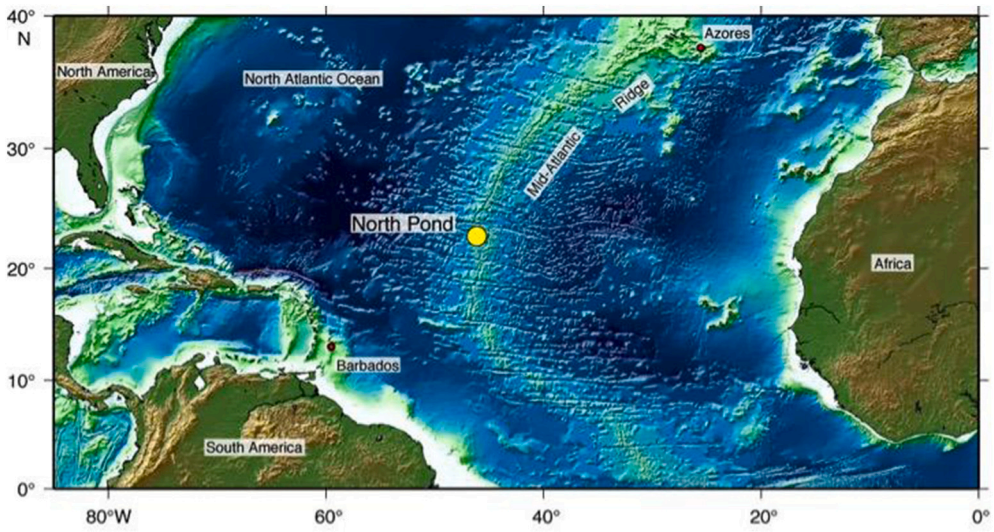


Fig. 1. Map showing the location of the sampling area, North Pond, marked by a yellow dot. Image credit: MBL. (For interpretation of the references to color in this figure legend, the reader is referred to the web version of this article.)

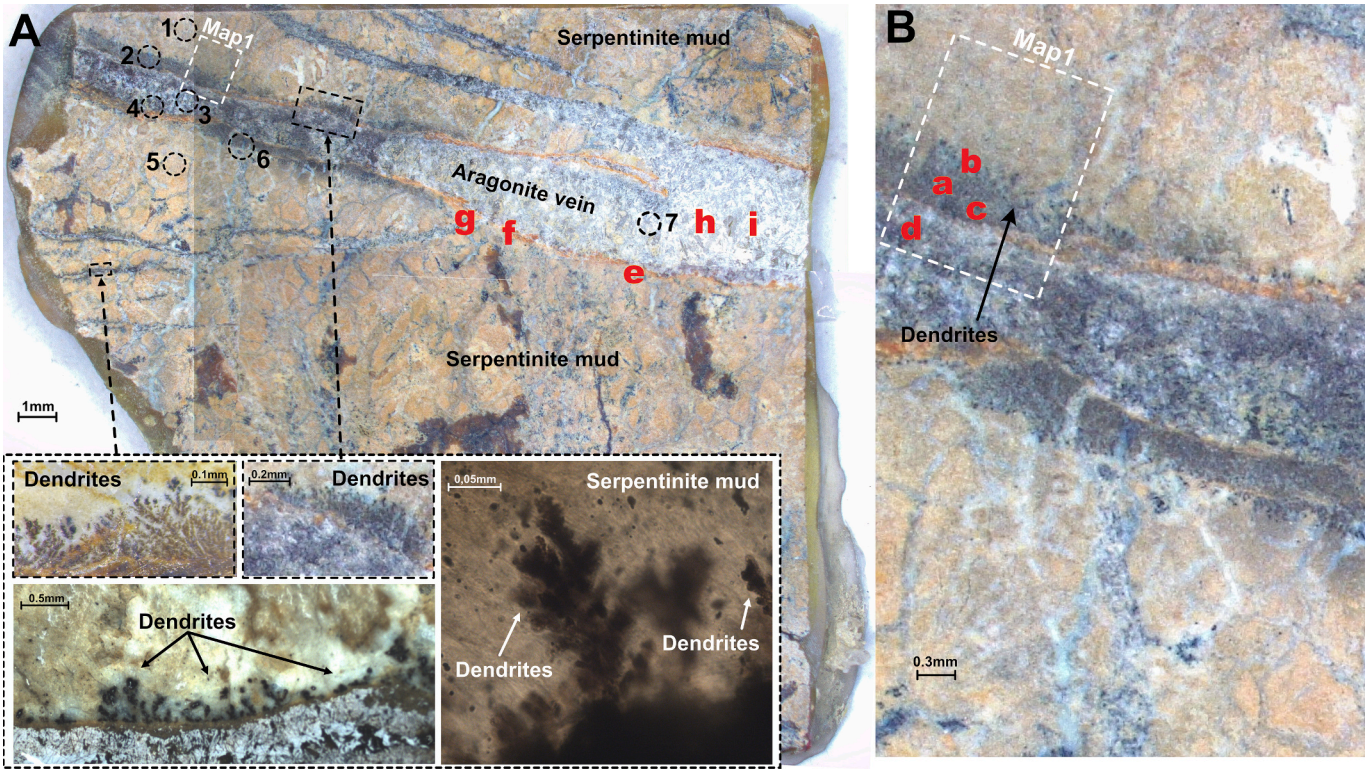


Fig. 2. Optical overview stitched image of the sample and its marked analyzed areas and spots. A) Some of the dendrites along aragonite veins are zoomed in as larger images in the lower, left side of the image, to illustrate the botryoidal, scallop-like shapes. The two analyzed maps are marked with dotted, white squares (see results Section 3.1). The microdrilled holes for δ^{60}Ni analyses are marked with numbers 1–7 (see Section 3.4). Letters a-i mark the microdrilled areas for δ^{13}C analyses (see Section 3.4). Area B, shows a zoomed in overview on the mapped areas.

2.2. Methods and analyses

2.2.1. Hyperprobe field emission electron probe microanalyzer- EPMA

Doubly polished thin sections (Ivarsson, 2006) and polished rock pucks were prepared from the samples to identify fossilized microorganisms and minerals using optical microscopy. Mineral chemistry and elemental distribution were analyzed using a Jeol JXA8530F Hyperprobe Field Emission Electron Probe Microanalyzer (EPMA) at Uppsala University, Sweden. Point analyses (in profiles) using Wavelength-dispersive X-Ray Spectroscopy (WDS) were conducted with a 10 nA beam current, 15 kV accelerating voltage, and 10 s peak/5 s background counting times at beam diameter of 5 μm. Chemical composition maps were generated also with WDS at 15 kV accelerating voltage, 40 nA beam current, 100 ms dwell time, 4 × 4 μm step size, and 4 μm beam diameter. All WDS analyses were standardized using wollastonite (for Ca, Si), pyrophanite (for Mn), hematite (for Fe), NiO (for Ni), MgO (for Mg). Achieved detection limit ranges (in ppm, based on results from points analyses in profiles) were: 25–48 for Ca, 61–108 for Si, 72–96 for

Mn, 68–96 for Fe, 66–85 for Ni and 34–55 for Mg.

2.2.2. Raman spectroscopy

Raman spectroscopy was performed at Uppsala University, Sweden, using a Renishaw InVia Reflex micro-Raman system equipped with a 1024-pixel RenCam CCD detector. A 532 nm laser source with plane-polarized light was employed, in combination with a 2400 lines/mm grating and a 50× objective lens (Numerical Aperture = 0.75). Spectral measurements were acquired with an absolute resolution of 1.7 cm^{-1}. Instrument calibration was conducted prior to each session using the characteristic 520.5 cm^{-1} Raman peak of a single-crystal silicon standard, yielding a relative spectral precision of ±0.12 cm^{-1}. The laser power at the sample surface was between 4 and 35 mW, verified by a Thorlabs PM160T power meter.

2.2.3. Ni isotope analyses and sample preparation

Samples and standards (NIST SRM 986, BHVO-2 and NIST SRM 976 for monitoring copper isobaric interferences), each containing 0.5–1 μg Ni, were evaporated on a hotplate. A double spike containing equal proportions of ^{61}Ni and ^{62}Ni was added to all samples and standards at a Ni_{sample}/Ni_{spike} ratio of 1 and re-evaporated to dryness. This double spike method corrects for instrumental mass bias and possible fractionation during chemical purification.

Rock powder samples were digested in HCl–HNO_3 mixtures in polytetrafluoroethylene vials, evaporated to dryness, and treated with HF (28 mol L^{-1}, trace metal or Suprapure grade) to dissolve any remaining solids. HF treatment was repeated after evaporation at 70–80 °C to ensure full digestion of silicate material and removal of fluorides. Ni concentrations were re-measured prior to Ni elution using an ICP-Quadrupole Mass Spectrometer (X-Series II, ICP-Q-MS) at Pôle Spectrométrie Océan, Brest. Aliquots (<1 mL) from water and rock solutions were diluted with 0.28 M HNO_3 to 10 mL total volume for quantification. The appropriate spike amount was recalculated based on these concentrations.

2.2.3.1. Sample purification. Sample purification methods are following the procedures outlined by Gueguen et al. (2013) at the Ifremer Centre de Bretagne, Brest, France. Dry sample–spike residues were dissolved in 1 mL of 0.24 M HCl. Subsequently, 0.3 mL of 1 M ammonium citrate and 125 μL of concentrated ammonia were added to raise the pH to 8. Approximately 0.5 mL of wet Ni-spec resin (Ni Eichrome) was placed into polypropylene columns, washed with 6.5 mL of Milli-Q water and 4.5 mL of 0.2 M ammonium citrate +0.45 M ammonia, and capped. An additional 0.5 mL of the 0.2 M ammonium citrate +0.45 M ammonia solution was added to buffer the resin pH to ~9. The sample solution was loaded onto columns containing dimethylglyoxime (DMG), which form a Ni–DMG complex between pH 8–9 and is retained in the resin. The resin was resuspended to increase the active surface area and left for 1 h, achieving near 100 % Ni yields. The columns were drained, and 2.2 mL of the 0.2 M ammonium citrate +0.45 M ammonia solution was added twice at 15-min intervals to wash out Fe and other elements. Then, 2.2 mL of Milli-Q water was added three times at 15-min intervals to remove excess salts. Ni was collected in 6.6 mL of 3 M HNO_3, added in three applications of 2.2 mL at 15-min intervals. The collected Ni fractions were dried on a hot plate at ~95 °C overnight and then dissolved in 1 mL of 0.3 M HNO_3 for isotope analysis.

2.2.3.2. Mass spectrometry. Nickel isotope compositions were analyzed using a Thermo Scientific™ Neptune multicollector inductively coupled plasma mass spectrometer (MC-ICP-MS) at the Ifremer Centre de Bretagne in Brest, France. Samples and standards were introduced through an ApexQ MicroFlow PFA-50 self-aspirating nebulizer at ~60 μL/min. Despite the use of Ni sample and skimmer cones, blank ^{58}Ni intensities confirmed no Ni contamination from the cones (as previously shown by Moynier et al., 2007; Fujii et al., 2011; Gueguen et al., 2013; Neubeck et al., 2021).

Samples were analyzed twice: initially with a short run (10 cycles, each 4 s) to determine Ni, Fe, and Cu concentrations. This step is essential before performing isotopic analyses, as accurate concentration measurements of these metals ensure proper correction for mass bias and matrix effects during isotope ratio analysis. Each sample had a matching standard with a similar concentration and Ni_{sample}/Ni_{spike} ratio. Samples were grouped in sets of 2–5, each set flanked by NIST SRM 986 as a bracketing standard. Procedure blanks were introduced as sets of 5 every 15th sample run.

In addition to NIST SRM 986, BHVO-2 was also used as a secondary reference material, especially for quality control and verifying the consistency of measurements across different sample sets. BHVO-2, a basaltic rock standard, provides a matrix similar to geological samples and serves as an additional benchmark for ensuring the accuracy of the isotope ratios.

High-precision isotope data were obtained in the second run, with each sample measured in five blocks of 10 cycles (4 s integration time per cycle) and a rinse between blocks. The instrument can precisely measure samples with Ni concentrations over 0.03 ppm, achieving 2SE < 0.1 ‰. Lower concentrations yield slightly larger uncertainties (2SE ≈ 0.1 ‰), and concentrations under 0.01 ppm have uncertainties >1 ‰ (Gueguen et al., 2013).

2.2.3.3. Ni isotope data reduction. Nickel isotope compositions of samples are expressed using the delta (δ) notation, in which the isotope ratio of the sample is normalized to that of the NIST SRM 986 bracketing standard, following the equation:

$$\delta^{60}Ni\ (‰) = \left[\left(^{60}Ni/^{58}Ni_{sample}\right)/\left(^{60}Ni/^{58}Ni_{SRM986}\right)\right]^{*} 1000 \quad (1)$$

The data presented in this study is described using the $^{60}Ni/^{58}Ni$ ratio given as $\delta^{60}Ni$. The Ni isotope compositions of samples were then calculated using the double spike calculation template from Gueguen et al. (2013). The NIST SRM 986 standard was passed through columns four separate times, yielding an average value and external reproducibility for the method.

2.2.4. Carbon isotopes

Carbon isotope analysis of micro-drilled samples was performed at the Stable Isotope Lab, SIL, at Stockholm University, Sweden. To determine the isotopic composition of total carbon ($\delta^{13}C_{tot}$), approximately 0.2 mg of solid precipitate powder was weighed and analyzed using a Flash Elemental Analyzer with Thermo Fischer isotope ratio mass spectrometer Delta V advantage (EA-IRMS). The international standards NBS-18, IAEA-CO-8 and IAEA-603 was used and measured approximately every 10th sample. And the long-term reproducibility for those are +/− 0.08 per mil (‰) for the last 10 years.

In-house standards used are Merck Calcium carbonate ($CaCO_3$) and a marble Carm, and the long-term reproducibility for Merck is ±0.12 ‰, and for Carm is +/− 0.08‰ for the last 10 years.

The $\delta^{13}C$ values are reported as ‰ deviations relative to the Vienna Pee Dee Belemnite (VPDB) standard, where $\delta^{13}C = (R_{sample} / R_{standard} - 1) \times 1000$, and R represents the $^{13}C/^{12}C$ ratio (Eq. (2)). Total carbon (TC) is expressed as weight percent of the initial sample mass. Based on repeated measurements of standards, the analytical reproducibility for $\delta^{13}C$ was ±0.06 ‰.

$$\delta^{13}C\ (‰) = \left(R_{sample}/R_{standard} - 1\right)10^{3} \quad (2)$$

3. Results

3.1. EPMA

The locations and corresponding EPMA elemental transect (Mn, Ni, Ca, and Fe) labeled A, B, and C are shown in Fig. 3. Another transect, D is

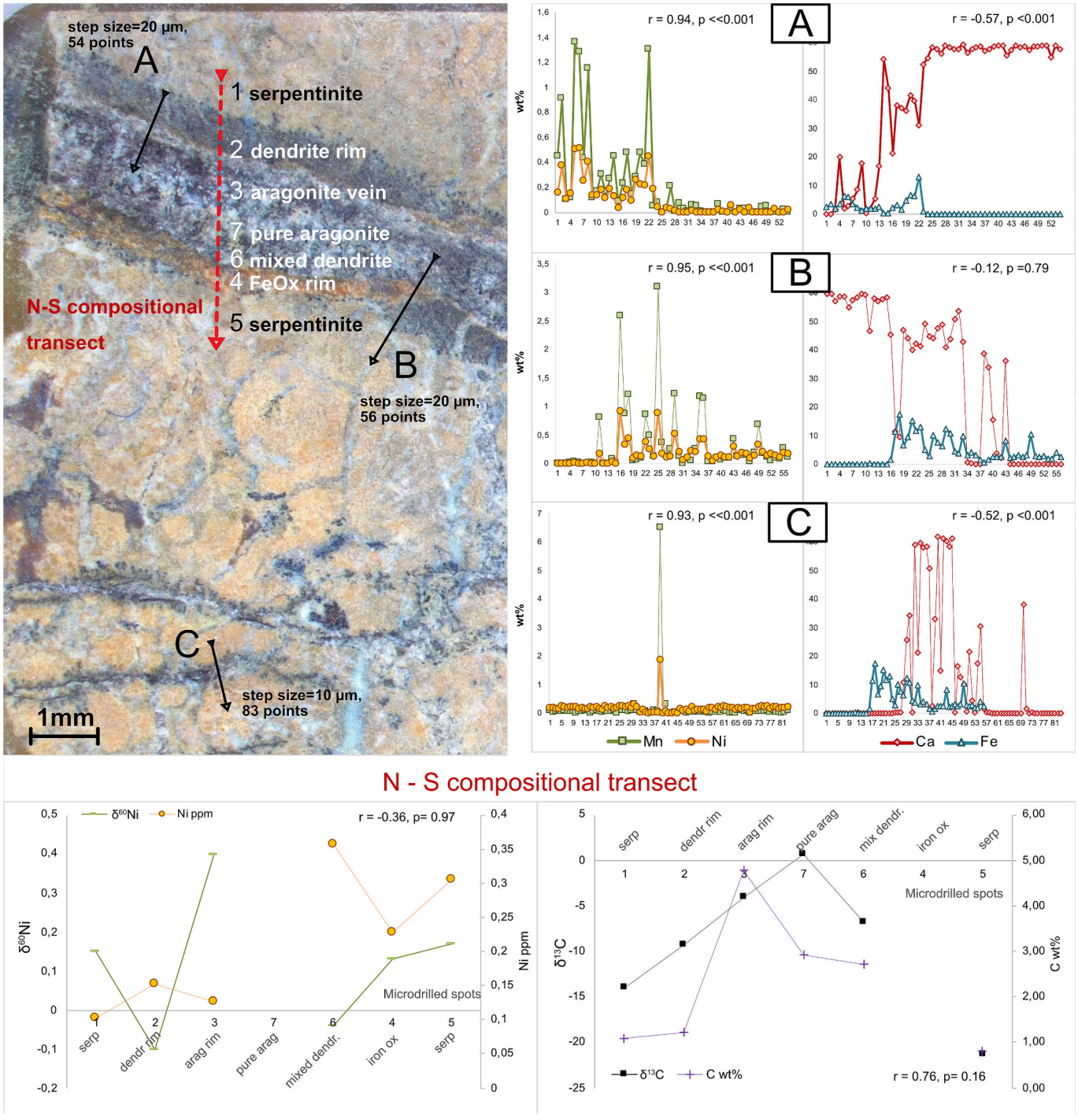


Fig. 3. Three EPMA transects (A, B, and C; left panel) cross dendritic structures associated with aragonite veins, highlighting compositional variations in Mn, Ni, Fe, and Ca within the serpentinite, aragonite veins, and dendritic regions (plots shown in the right panel). A projected N—S compositional transect (bottom panel), based on the sequence of spot analyses (see Table 1 and Table S1), illustrates trends in elemental concentrations and isotopic compositions in relation to the veining system.

shown in Fig. 4. Transect A intersects the Mn—Fe dendrites and extends into the aragonite vein. The transition from dendritic material to aragonite is evident in the elemental profiles, where Mn and Ni concentrations are significantly higher in the dendritic rim compared to the aragonite vein. Iron is also slightly enriched in the dendritic rim and approaches zero in the aragonite. Transect B crosses a zone of aragonite, mixed dendritic material, and serpentinite. Here, Mn, Ni, and Fe concentrations peak in the mixed dendritic zone, are lowest in the aragonite, and show intermediate levels within the serpentinite matrix. Transect C cuts through serpentinite containing a very thin aragonite vein with dendritic structures, which appear as sharp spikes in Mn and Ni concentrations in the elemental data (Fig. 3, Table S1). Transect D cuts through serpentinite, dendrites, and into the aragonite vein (Fig. 3; S3, Table S1). The serpentinite is characterized by high Mg and Si, the dendrites by elevated Ni, Mn, and Fe, and the aragonite vein by high Ca but low Mg and Si.

Pearson correlation analysis (Table 1) across all transects reveals positive correlations between Mn and Ni, Fe and Ni, and Mg and Ni. In contrast, Ca shows negative correlations with both Fe and Ni. The strongest correlation is observed between Mn and Ni, with all three

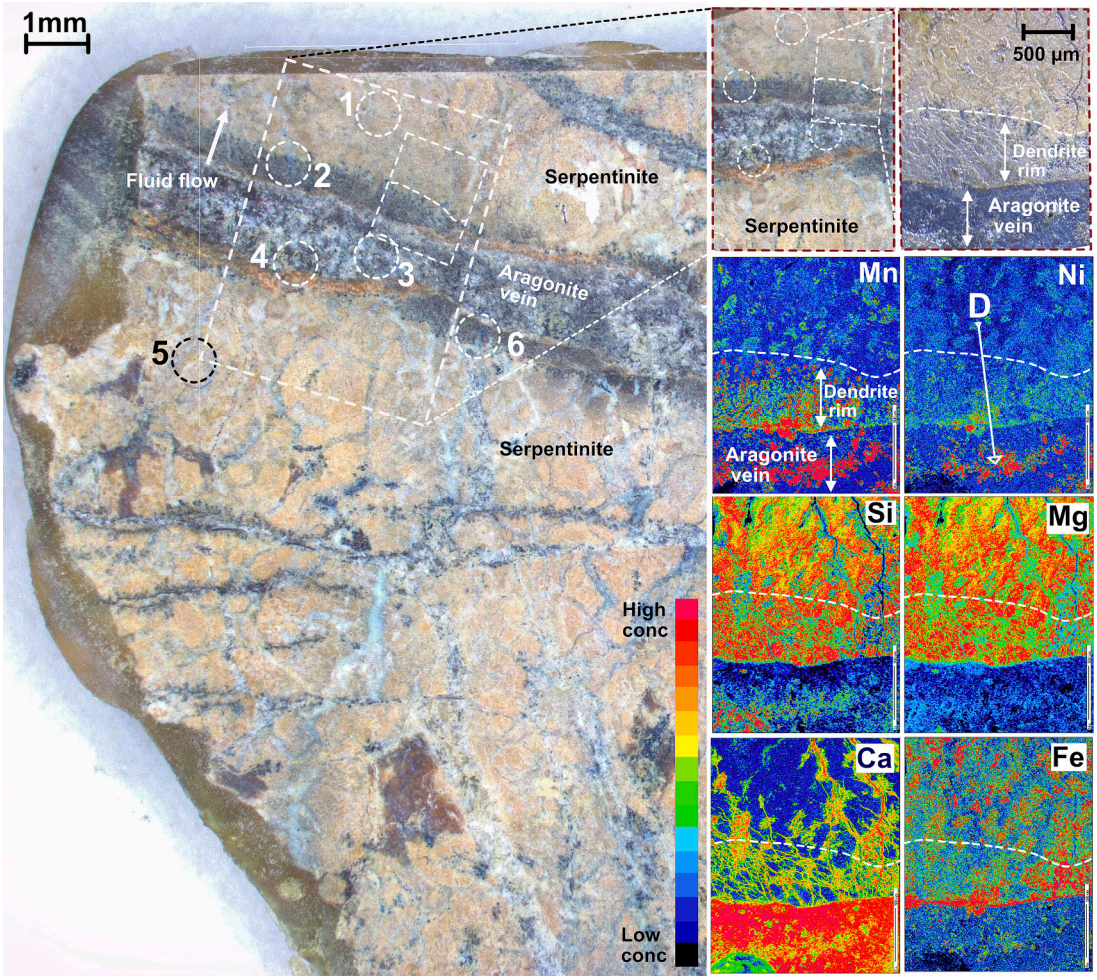


Fig. 4. Overview optical image showing the serpentinite with the crosscutting aragonite veins and fake color EPMA maps. The dark gray rim on the vein edges is marked here as "dendrite rim" since these contain the Fe—Mn dendrites. The yellowish, brownish rim contains less Mn and more iron oxides (Table 1, Fig. 3). To the right, fake color, intensity EPMA maps are shown to illustrate elemental distribution. The maps show relative signal intensity differences from the highest (red) to the lowest (blue) or nearly none (black) measured in the area for each element, where red color represents high abundance of the element and black low abundance. Absolute elemental (Mn, Ni, Si, Mg, Ca and Fe) abundance (wt%) of the serpentinite, dendrites and aragonites based on the transect D (in the Ni EPMA map) can be found in table S1. The oxidizing fluid direction is marked with an arrow.

transects yielding p-values $<< 0.001$.

To investigate spatial trends in element distributions, a projected N—S geochemical transect was constructed by ordering the analyzed spots as follows: 1, 2, 3, (7), 6, 4, 5 (cf. Table 1, Fig. 3), representing the serpentinite, dendrite rim, aragonite vein, pure aragonite, mixed dendrite, the Fe-rich dendrite and serpentinite, respectively. Along this transect, δ^{60}Ni, Ni (ppm), δ^{13}C, and C (wt%) were plotted to identify systematic compositional variations in relation to mineralogical features and the veining system, although the number of analyzed spots were too limited to establish statistically robust correlations.

EPMA element maps show that Mn-dendrite rich regions form a distinct rim between the carbonate vein and the serpentinized host rock, characterized by high concentrations of Fe, Ni, and Mn (Fig. 4, Fig. S1). The highest Ni concentrations are found in the central parts of the carbonate vein and within the Mn-dendrites, gradually decreasing towards the serpentine. While Ca levels decrease towards the center of the aragonite vein, Si, Ni and Mn concentrations increase. The large vein that intersects the serpentine has somewhat elevated levels of Ni, Mn, Fe, and Ca, but lower levels of Si and Mg compared with the serpentine. The Mn concentration gradually decreases inward towards the serpentine. The smaller veinlets are dominated by Ca, Ni and Fe.

3.2. Raman spectroscopy

The Raman peaks of the dendrites show two major peaks around 503 and 630 cm^{-1}, corresponding to Mn—O asymmetric stretching vibrations and Mn—O bending and stretching modes (Ostrooumov, 2017). The peaks at 1430 and 1630 cm^{-1} are associated with bound water, C═C stretching modes, and/or metal oxides (Fig. 5).

3.3. Nickel isotopes

The Mn-rich regions of the sample (Figs. 3, 4, 5 and Fig. S1) exhibited marginally negative δ^{60}Ni values between -0.10 ± 0.05 and -0.04 ± 0.03 ‰, whereas the serpentine displayed heavier isotope signatures around δ^{60}Ni $= +0.15 \pm 0.03$ ‰. The pure vein aragonite lacked sufficient Ni content for isotope measurement, although the vein adjacent to the Mn dendrites displayed δ^{60}Ni values of δ^{60}Ni $= +0.40 \pm 0.13$ ‰. δ^{60}Ni is negatively correlated with Ni concentration (Fig. 3), whereas Ni and Mn show a positive correlation. Transect A exhibits a correlation coefficient of 0.94 ($n = 54$, $p << 0.005$), Transect B 0.95 ($n = 56$, $p << 0.005$), and Transect C 0.93 ($n = 83$, $p << 0.005$).

Table 1
Pearson correlation coefficients (R), t-values, and p-values for elemental relationships along EPMA transects A, B, and C (cf. Fig. 3), as well as variable trends for Fe, Mg, and Ca in relation to Ni and Fe. The middle part of the table shows δ^{60}Ni, Ni (ppm), δ^{13}C, C (wt%), and Fe (ppm) values used for the projected N—S geochemical transect (cf. Table 1, Fig. 3), constructed from spot analyses. The analyses marked with an asterisk are literature values from Neubeck et al., 2021. The lower part of the table shows EPMA measured Ni, Mn and Fe spots A-I (cf. Fig. 2) in wt%.

Elements	Transect	R	t-value	p-value
Ni vs Mn	A	0,94	20,80	0,000
	B	0,95	21,57	0,000
	C	0,93	19,17	0,000
Ca vs Fe	A	-0,57	-4,99	0,000
	B	-0,12	-0,86	0,786
	C	-0,52	-4,49	0,000
Fe vs Ni	A	0,84	11,28	0,000
	B	0,40	3,22	0,004
	C	0,17	1,23	0,446
Mg vs Ni	A	0,69	6,84	0,000
	B	0,11	0,81	0,842
	C	0,08	0,57	1,143
Ca vs Ni	A	-0,75	-8,06	0,000
	B	-0,25	-1,86	0,136
	C	-0,17	-1,27	0,416
Fe vs Mn	A	0,80	9,56	0,000
	B	0,24	1,85	0,140
	C	-0,10	-0,70	0,972

Comp. transect	δ^{60}Ni	Ni ppm	C wt%	δ^{13}C	Fe ppm
Serp (#1)	0,15 ± 0,03	0,10	4,52	-14,01	1,83
Dendr (#2)	-0,1 ± 0,05	0,15	5,07	-9,25	0,81
Arag vein (#3)	0,4 ± 0,07	0,13	19,85	-4,02	0,20
Pure arag (#7)			*12,15**	*0,67**	
Mix dendr (#6)	-0,04 ± 0,03	0,36	11,29	-6,75	4,31
FeOx rim (#4)	0,13 ± 0,04	0,23			3,32
Serp (#5)	0,17 ± 0,03	0,31	2,93	-21,32	5,08

EPMA Spots	Sample	Ni (wt%)	Mn (wt%)	Fe (wt%)
Dendrites	A	0,54	1,78	6,11
Dendrites	B	0,69	1,81	8,34
Dendrites	C	0,56	2,85	0,49
Vein center	D	0,35	1,71	0,32
iron oxide rim	E	0,67	1,31	0,60
Iron oxide rim	F	0,20	0,13	9,91
iron oxide rim	G	0,16	0,06	6,57
Aragonite	H	0,02	0,03	0,01
Aragonite	I	0,02	0,03	0,03

3.4. Carbon isotopes

The carbon isotopes showed an average serpentine value of $\delta^{13}C = -17.67 \pm 5.17$ ‰ $\delta^{13}C = -4.02$ ‰ for the aragonite vein, $\delta^{13}C = -9.25$ ‰ for the pure dendrites and $\delta^{13}C = -6.75$ ‰ for a mixture of serpentine and dendrites (however mostly dendrites), see Table 1, Fig. S4. The carbon isotopes show no direct correlation with C (wt%, Fig. 3), likely due to the limited dataset.

4. Discussion

Fe—Mn dendrites observed in serpentinites are striking mineral features that can potentially provide insights into fluid-rock interactions, redox conditions, and even microbial activity. This study investigates dendrites from IODP Site 1272 A, focusing on their growth patterns, morphology, chemical composition, and isotopic signatures to evaluate whether their origin is biogenic or abiotic.

4.1. Inward-growing Fe—Mn dendrites in serpentinites

The Mn-rich dendrites differ from those observed at other depths within the same drill core (Neubeck et al., 2021), as they extend from open veins inward towards the serpentinized host rock (Fig. 2). This contrasts with previously described dendrites that grow outward from serpentine into the vein space, which is later infilled by aragonite (Ivarsson et al., 2018; Neubeck et al., 2021).

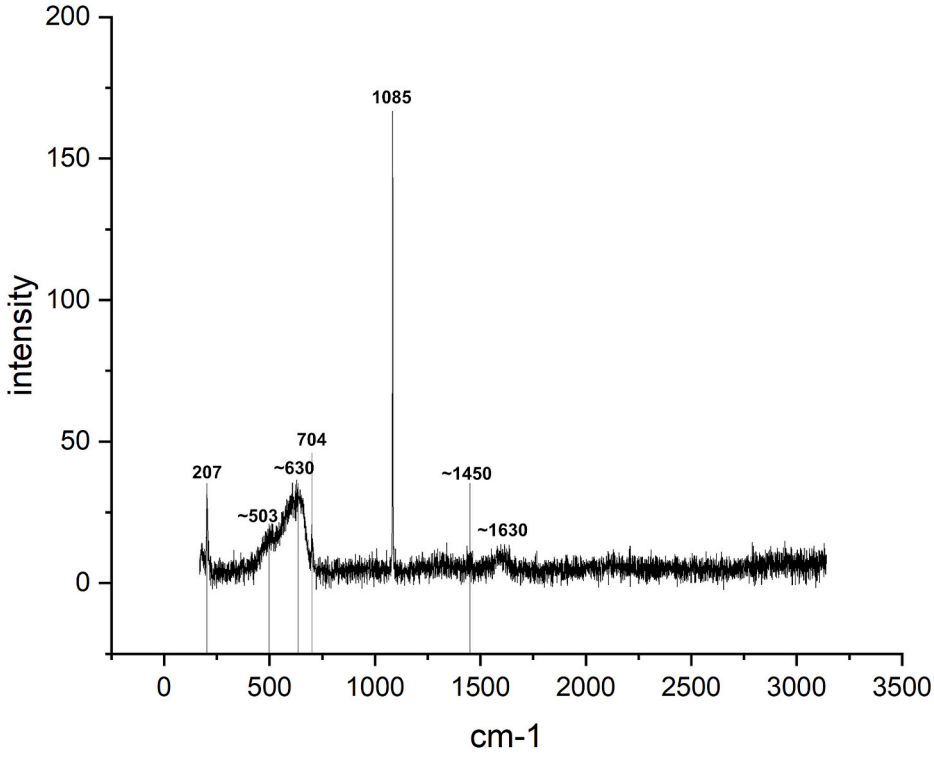


Fig. 5. Raman spectrum of aragonite (207, 704 and 1085 cm^{-1}) and Mn oxides (503 and 630 cm^{-1}). The 1450 and 1630 cm^{-1} peaks represent C═C, water, and/or oxide lattice vibrations. Iron oxides (hematite and maghemite) with peaks around 500–550 and 700 cm^{-1} may partly overlap with the Mn spectrum.

Earlier studies have interpreted associated microstromatolites and filamentous morphologies as biogenic, based on a combination of morphological characteristics, low formation temperatures, and stable carbon isotope data (Benzerara and Menguy, 2009; Ivarsson, 2006; McLoughlin et al., 2007). Additionally, it has been proposed that microbial communities, comprising bacteria and fungi, may play a role in the formation or modification of Fe—Mn dendrites (Sjöberg et al., 2021), particularly in serpentinized environments with temperatures below ~14 °C (Alt et al., 2007b), where such microorganisms could colonize fractures and later become preserved within carbonate phases.

4.2. Mineralogy

Mineralogically, the dendrites are composed of disordered Fe and Mn oxides (Figs. 3, 5) growing into the serpentinite (Fig. S3) from an aragonite-dominated vein (Fig. S2). Raman spectroscopy reveals two major peaks at approximately 503 and 630 cm^{-1} with putative, weak shoulder at ~570–580 cm^{-1} (Fig. 5), corresponding to Mn—O asymmetric stretching and bending/stretching modes, respectively, which are consistent with birnessite (Ivarsson et al., 2018; Neubeck et al., 2021; Ostrooumov, 2017). These results resemble Raman spectra of synthetic birnessites formed at ~150 °C (Saenko, 2024), similar to the low-temperature serpentinization conditions of this sample (Alt et al., 2007). The 630 cm^{-1} peak is broad, possibly indicating overlapping features from additional phases such as Fe—O stretching in maghemite or hematite (~500 cm^{-1}) and Fe-OH bending in hausmannite or hematite (~650 cm^{-1}) (Chernyshova et al., 2007). According to extensive Raman investigations by Bernardini et al. (2019, 2020, 2021a, b, 2024, 2025) on natural manganese oxides, these phases commonly exhibit prominent Raman bands near 490 and 625 cm^{-1}. Bernardini et al. (2020) further demonstrated that Raman spectroscopy can reliably distinguish the oxidation state and coordination environment of Mn, based on the position and shape of the ν_1 modes. The $\nu_1[6]Mn^{4+}$ notation refers to the symmetric stretching vibration (ν_1) of Mn^{4+} situated in sixfold (octahedral) coordination. In their detailed study of a wide range of well-characterized Mn oxide samples, Bernardini et al. (2020) showed that the $\nu_1[6]Mn^{4+}$ band typically occurs near 650 cm^{-1} in phases with empty structural channels, but shifts to ~630 cm^{-1} when large cations occupy the channels. The presence of this lower-frequency band in our spectra suggests a similar structural configuration, likely involving the incorporation of Fe^{3+} and Ni^{2+} (Fig. 3), which necessitates partial $Mn^{4+} \rightarrow Mn^{3+}$ substitution to preserve charge balance. Raman spectroscopy can reveal Mn oxide mineral phases and Mn oxidation states, offering indirect clues to biogenicity (Bernardini et al., 2021a, 2021b). However, similar spectral features can arise in both biogenic and abiotic Mn oxides, making clear distinctions difficult (Huld et al., 2023). The Raman bands observed around 1450 cm^{-1} and 1630 cm^{-1} are commonly attributed to hydrocarbon-related compounds (Romero-Sarmiento et al., 2014) and poorly ordered or amorphous carbon (Beyssac et al., 2002), respectively. These features suggest the presence of thermally altered or mildly matured carbonaceous material (Beyssac et al., 2002, 2003), consistent with previous observations from similar samples (Neubeck et al., 2021), here suggesting an influence (direct or indirect) of biology on the dendrites. The absence of typical carbon bands, such as the D band (~1350 cm^{-1}), the G band (~1580 cm^{-1}), and the overtone/combination bands in the 2700–3100 cm^{-1} region (associated with sp^2 carbon bonding and graphitic structures), indicate that the material is not highly graphitized and likely lacks well-ordered crystalline carbon (Beyssac et al., 2002, 2003).

4.3. Manganese oxidation states

Manganese(IV) oxides are prevalent in most environments and typically form through the biotic oxidation of Mn(II) by O_2, a process mediated by microorganisms and generally faster than abiotic mechanisms (Sjöberg et al., 2021, Bernardini et al., 2021a, 2021b). However, under certain conditions, such as elevated pH, low microbial activity, and the presence of nano-sized mineral surfaces like ferrihydrite, abiotic Mn(II) oxidation can also play a significant role in producing Mn(III/IV) (oxyhydr)oxides (Wang et al., 2015). Wang et al. (2015) showed that

ferrihydrite surfaces enhance Mn(II) oxidation, promoting the formation of stable phases such as manganite, hausmannite, and birnessite over less stable ones like feitknechtite or groutite. These reactions are influenced by factors including pH, Mn(II) concentration, and O_2 levels, which collectively determine the oxidation state and crystallinity of the resulting Mn oxides.

While biogenic processes often yield poorly crystalline birnessite-like Mn(IV) oxides, abiotic pathways, particularly those catalyzed by mineral surfaces, may account for much of the observed mineralogical diversity. Co-precipitation with iron oxides in these settings also has implications for contaminant mobility, underlining the environmental relevance of surface-catalyzed abiotic (Bernardini et al., 2021a, 2021b; Tebo et al., 2004; Madden and Hochella, 2005; Junta and Hochella, 1994).

Hematite surfaces can similarly catalyze Mn^{2+} oxidation in the presence of dissolved O_2, with nanoscale hematite significantly accelerating the reaction (Madden and Hochella, 2005). This enhancement is linked to size-dependent shifts in electronic structure, including increased Lewis basicity of surface oxygen atoms and a higher density of reactive sites such as edges and kinks. Electron transfer theory attributes the higher reaction rates to stronger electronic coupling and lower reorganization energy, particularly at sites where Mn^{2+} coordination deviates from its usual octahedral geometry (Madden and Hochella, 2005).

Although there is evidence for the abiotic formation of Mn oxides, microbially mediated processes often result in the production of similar Mn^{3+}/Mn^{4+} phases, complicating the distinction between biotic and abiotic pathways in natural systems (Jung, 2017). Consequently, both mechanisms are likely involved in Mn oxide formation. Abiotic processes may dominate in environments enriched in nanoparticles, catalytic mineral surfaces, or where photo-oxidation is possible (Jung, 2017). However, in deep subsurface settings, where photochemical oxidation cannot occur (Jung, 2017), microbial mediation and/or catalytic mineral surfaces (including nanoparticles) is likely to play a significant role in Mn^{2+} oxidation and the subsequent precipitation of manganese oxides (Bernardini et al., 2021a, 2021b).

4.4. Viscosity contrast dendrites

Despite these suggestions, the precise mechanisms responsible for Fe—Mn dendrite formation in serpentinized rocks remain poorly understood. To date, only a limited number of studies have focused on natural three-dimensional Fe—Mn dendrites (Hou et al., 2023; Garcia-Ruiz et al., 1994; Chopard et al., 1991) or their carbon isotopic signatures (Neubeck et al., 2021). Hou et al. (2023) demonstrated that dendrites in clinoptilolite tuffs may form via the accretion of Fe—Mn oxide nanoparticles at the interface between Fe-Mn-rich and oxygenated fluids, with fluid mixing dynamics and viscosity contrasts playing a critical role. Nanoparticles are hypothesized to form when an infiltrating fluid displaces oxygenated pore water and mixes with it, producing a Mn-oxide-oversaturated solution. Laboratory studies have shown that such conditions favor the nucleation of Mn-oxide nanoparticles (Li et al., 2014; Huang et al., 2015). A comparable mechanism is plausible for the dendrites documented in Sample 1272 A. The dendrites observed here resemble those of Hou et al. (2023), showing a primary trunk with a botryoidal surface and scallop-like top (Fig. 2). While this morphology supports an abiotic nanoparticle accretion model, it does not exclude the possibility that the initial nucleation of particles could be biologically mediated. Indeed, as discussed in previous work, abiotic and biogenic Mn dendrites often share similar mineralogical and structural features, making it challenging to definitively determine their origin without multiple lines of supporting evidence.

The Raman-EPMA element maps revealed an association of carbonate with silica in the central parts of the vein (Fig. S1), suggesting infiltration of oxidizing, CO_2-rich fluids in the serpentines, resulting in leaching and reprecipitation of silica (Buckman and Ashley, 2010), similar to successive fluid-driven reactions of serpentinized peridotites (Boskabadi et al., 2020). The plastic, clay-like and high viscous character of the serpentine reported in Bach et al. (2004) in contact with the oxidizing low viscous fluids may have provided a particularly suitable mechanism for formation of dendrites, through the so called “viscous fingering” mechanism (Garcia-Ruiz et al., 1994; Suekane et al., 2017, 2019). Viscous fingering involves the formation of dendritic patterns when a less viscous fluid (LVF) displaces a more viscous fluid (MVF), resulting in the formation of dendritic “fingers” due to differences in density. In the study by Hou et al. (2023), similar 3D mineral dendrites in clinoptilolite are described as arising from the interaction between fluids and chemical gradients and, like those discussed here, grow perpendicular to the direction of the crack or vein. Parts of the vein wall has a brownish, yellowish rim where the dendrites are located and which is richer in Fe oxides (Figs. 2, 3, Table 1, table S1). A plausible formation process for these dendrites begins with the initial serpentinization of the host rock, producing serpentinite mud (Bach et al., 2004). As proposed by Bach et al. (2004), low-temperature alteration may have postdated serpentinization, consistent with our observations of an earlier episode of serpentinization of harzburgite and dunite into serpentinite muds. During this process, Mn^{2+} released from the alteration of primary silicates could have remained in solution. Subsequent episodes of low-viscosity, oxidizing hydrothermal fluids likely transported and precipitated Mn oxides within the mud. These fluids infiltrated the higher-viscosity serpentinite mud, forming dendritic Mn oxides along pressure gradients marking a fluid flow (Fig. 4). The interaction between two fluids of different viscosity would also explain why these dendrites are growing “inwards” rather than outwards into the carbonate vein, which have been reported in previous samples (Ivarsson et al., 2018; Neubeck et al., 2021). The low viscosity alteration fluids most likely were also enriched in Mn and Ni compared with host serpentine and as evidenced in Fig. 3 and Table 1, the majority of the Mn is found in the veins and vein rims and decline in concentration inwards, towards the serpentine (transects A-D, Figs. 3, 4, S3).

4.5. Dendrite morphology

Dendrites exhibit a wide range of morphological changes depending on the environmental conditions. In viscous fluids, the growth patterns are significantly influenced by the viscosity of the medium. Higher viscosity fluids tend to suppress the growth of dendrites by reducing the rate of diffusion and convection, leading to more compact and less branched structures (Jeong et al., 2001). Conversely, in low-viscosity fluids, dendrites often develop more intricate and branched morphologies due to the enhanced mobility of solutes and the formation of natural convection currents (Hou et al., 2023, Eshraghi et al., 2017). In deep sea, the morphological changes are further complicated by the interaction of oxygenated fluids with the matrix. The influx of oxygenated fluids can lead to the formation of Liesegang stripes and fractal dendrites, which are characteristic of non-equilibrium conditions (Liu et al., 2023). These patterns are often observed in rocks such as limestone and sandstone, where the precipitation of minerals occurs under varying diffusion parameters and material properties (Liu et al., 2023).

Several groups have studied the formation of different crystal morphologies as an attempt to understand the diverse crystal structures found in similarly composed rocks (Bogoyavlenskiy and Chernova, 2000; Oaki and Imai, 2003; Saito and Ueta, 1989). The dendritic character of crystals is commonly associated with and out-of-equilibrium, diffusion-controlled process with an unstable growing surface, the contact between fluids of different densities or viscosities (Garcia-Ruiz et al., 1994) or, a fluid in contact with a high porosity rock. An equilibrium situation will form single polyhedral crystals, whereas out-of-equilibrium will shift the morphology towards irregular dendrites formed by polycrystalline aggregates and the chemical composition has been suggested to have a limited effect on morphology (Liu et al., 2023). Rather, viscosity differences and diffusion rates control the morphology

(Liu et al., 2023). The increased concentration of Mn at the dendrite tips (Fig. 4) may be explained by: (i) a concentration gradient, where oxygenated fluids oxidize more Mn at the growth front or dendrite tips; (ii) a geometric effect, where a cross-section of the dendrites gives the appearance of higher Mn concentrations in the walls compared to the nearly hollow interiors; or (iii) the progressive growth of manganese-oxidizing microorganisms extending inward into the serpentine mud. However, microorganisms typically grow towards sources of energy, making the scenario described by Neubeck et al. (2021) plausible, where microbial colonies attach to vein walls and extend outward into the vein, benefiting from continuous fluid flow that supplies fresh nutrients. In contrast, it is less intuitive to envision why microorganisms would grow inward into the serpentine mud. Nevertheless, the presence of organic carbon (Fig. 5), morphological similarities to other dendritic structures (Sjöberg et al., 2021; Neubeck et al., 2021), and the slightly negative carbon isotope values (Table 1) together suggest at least some degree of microbial involvement.

4.6. Dendrite growth environment

The environment of growth may be a primary factor accounting for the different dendrites including their isotopic compositions. In Neubeck et al. (2021), the dendrites grew into the vein later filled with aragonite, whereas the dendrites described in this study grow into serpentine mud. One explanation for the chemical differences between these two types of Mn-rich dendrites may be the type of mineralization process that is involved. According to Dupraz et al. (2009), four biomineralization processes may account for different types of dendrites; a) biologically controlled biomineralization (BCM) where organisms exert precise control over the mineralization process, including the location, timing, and type of minerals formed, b) biologically induced biomineralization (BIM), where the environment created by organisms indirectly influences mineral formation, often as a byproduct of metabolic activities, where organisms alter their local environment to facilitate mineral deposition, c) intracellular biomineralization where minerals form within the cells and d) extracellular biomineralization where the minerals form outside the cells. The different dendritic structures in this study might all be influenced by microbial activity, but result from various biomineralization processes. For instance, aragonite dendrites, which contain organic carbon and light carbon and nickel isotopes, might be biologically induced. On the other hand, serpentine dendrites, with heavier carbon isotopes and slightly negative nickel isotopes, might be partially induced by biological activity and partially formed through non-biological processes. In this scenario, a microbial "seed", such as a living cell, organic matter, or extracellular polymeric substance, could initiate the otherwise abiotic precipitation of Mn oxides (Jung, 2017; Sjöberg et al., 2021). This seed could promote ion entrapment and oxidation, particularly of Mn^{2+}. Alternatively, the process may be entirely abiotic, beginning with the formation of a nucleating nanoparticle and followed by the progressive precipitation of Fe—Mn oxides (Jung, 2017). Abiotic formation of the Mn oxides, such as birnessite, may have fractionated the stable nickel isotopes through adsorption and/or coprecipitation (Sorensen et al., 2020). The dendritic microstromatolites documented in previous papers (Neubeck et al., 2021, Ivarsson et al., 2018) showed a cyclic growth pattern, visible as laminations within the dendritic shapes, which has not been observed in our serpentine dendrites, also indicating another formation process.

4.7. Nickel isotopes and manganese oxides

Nickel isotope analyses were conducted on dendrites using microdrilling and well-established methods yielding δ^{60}Ni values of −0.10 ‰ and − 0.04 ‰ (Table 1, Fig. 2). The δ^{60}Ni values revealed a lighter isotope signature associated with the Fe-Mn-rich dendrites while the inner aragonite vein parts and the serpentine muds displayed heavier δ^{60}Ni values of +0.40 ± 0.07 ‰ and + 0.16 ± 0.03 ‰, respectively. However, all these values are still considerably lighter than the average seawater values of ~1.4 ‰ (Archer et al., 2020; Cameron and Vance, 2014; Takano et al., 2017) but within the range shown in igneous and mantle-derived rocks (−0.19 and + 0.37 ‰, respectively, Cameron et al., 2009, Gueguen et al., 2013, Gall et al., 2017). The values also fall within the reported isotopic range of weathered ultramafic and mafic rocks (−0.60 to +0.30 ‰, Ratié et al., 2015, Spivak-Birndorf et al., 2018). However, the values are heavier than the hydrothermal values reported by Pašava et al. (2019) from the pyrite dominated Logachev hydrothermal crust (−0.24 ‰) and more in line with the Logachev serpentinites (−0.13 ‰) reported by Gueguen et al., 2013, suggesting a similar alteration process. All values are additionally considerably heavier than any reported biogenic Ni, see Fig. 6 below but similar to δ^{60}Ni values in black shales, which are rich in organic matter and often associated with Mn phases (Dong et al., 2023).

Previous measurements of hydrogenetic marine ferromanganese crusts have reported values ranging between +0.9 to +2.5 ‰ (Gueguen et al., 2021 and Gall et al., 2013, Fig. 6), which deviates from the values presented here. Although Mn nodules are often studied, they account for only a small fraction (0.1 %) of the total Mn deposited in the ocean (Fleischmann et al., 2023). Consequently, other Mn-rich deposits, such as sediments and serpentine muds, may play a more substantial role in controlling the overall marine Ni budget, particularly through Ni scavenging and isotope fractionation (Fleischmann et al., 2023). The strong correlation between Mn and Ni (Fig. 3, Table 1) and the negative correlation between δ^{60}Ni and Ni (ppm), show that Mn-oxides are strong scavengers but also that they preferentially scavenge the lighter Ni isotopes. It is unclear however, if our δ^{60}Ni isotope values are idicative of a abiotic or biologic signature. Fleischmann et al. (2023) demonstrated this with a comprehensive Ni isotope dataset for modern Mn- and organic-rich pelagic sediments, reporting values from −0.20 to 0.09 ‰, consistent with our findings. Our data suggest that these light Ni signatures are preserved over time in hydrothermally derived and tectonically emplaced rocks, such as the serpentinites analyzed in this study. The noticeably lighter δ^{60}Ni values associated with our Fe-Mn-rich dendrite rim of −0.10 ± 0.05 ‰ and − 0.04 ± 0.03 ‰, respectively, compared with the Fe-richer oxide rim of +0.13 ± 0.04 ‰ also suggest that Mn oxides is a stronger scavenger of light Ni than the more Fe-rich oxides, because of the strong sorption properties of Mn oxides such as birnessites (Peacock and Sherman, 2007a, 2007b). The correlation between Ni and Mn is also stronger than the correlation between Fe and Mn (average 0,94 vs average 0.47, Fig. 3, Table 1, table S1). Natural Mn oxides often have large surface areas, low point of zero charges, high negative charges, and high reduction potential, compared with for example iron oxides, making them exceptional scavengers of cations such as Ni (Li et al., 2024). This is evident also in our data, where the Ni abundance is closely following the abundance of Mn (transects in Fig. 3) and where the correlation between Mn and Ni is 0,94 (Table 1, table S1). The strong fractionation capacity of Mn oxides has been investigated through abiotic, laboratory experiments by Sorensen et al. (2020), who showed Ni fractionation factors ($\Delta^{60/58}Ni_{min\text{-}aq}$) as low as −3.35 ‰, which are values not yet found in natural environments. Commonly, Ni isotopes in Mn oxides are relatively heavy (Fig. 6) and the reported heavy δ^{60}Ni of hydrogenetic ferromanganese crusts (Gueguen et al., 2021; Gall et al., 2013) and the light δ^{60}Ni values of laboratory experiment birnessites showed by Sorensen et al. (2020), demonstrate the complexity of Ni isotope fractionation mechanisms in Mn rich minerals. Little et al. (2020) investigated the fractionation of Ni isotopes during diagenetic remobilization processes, focusing on the role of Mn oxides. Their study highlights how the dissolution and precipitation cycles of Mn oxides, coupled with mineralogical transformations from birnessites to todorokites, can account for the observed light Ni isotopic compositions in hydrogenetic Fe—Mn crusts and metalliferous sediments in the eastern Pacific. Additionally, the research suggests that Fe oxides contribute to the lighter Ni isotopic values, which we observed in the Fe—Mn dendrites, due to the mixed mineralogical composition of Fe and

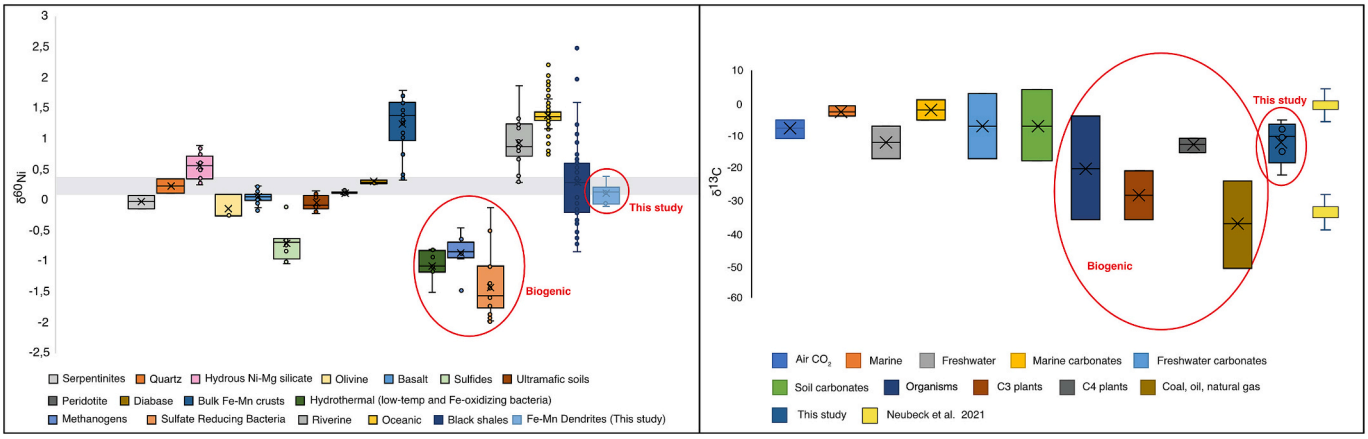


Fig. 6. Literature values of δ^{60}Ni (left panel) and δ^{13}C (right panel) in natural and laboratory samples. References: Spivak-Birndorf et al., 2018, Gall et al., 2012, 2013, Gueguen et al., 2013, 2021, Ratié et al., 2015, Ratnayake et al., 2021, Wang et al., 2021, Klaver et al., 2020, Li et al., 2021, Beunon et al., 2020, Chernonozhkin et al., 2015, Steele et al., 2011, Chen et al., 2023, Cameron et al., 2009, Cameron and Vance, 2014, Lemaitre et al., 2022, Archer et al., 2020, Sorensen et al., 2020, Pašava et al., 2019, Hein et al., 2013, Wagner et al., 2018, Neubeck et al., 2021). The gray area represents the BSE $\delta^{60/58}$Ni value modified from Hiebert et al., 2022).

Mn oxides present in these structures (Fig. 3, Table 1, table S1). However, the correlation between Ni and Fe across the transects show mixed results where only one of the transects show a strong correlation (0.84, $n = 54$, $p < <0.005$, Fig. 3, Table 1). Little et al. (2020) reported δ^{60}Ni values of −0.8 ‰ in metalliferous sediments in the east Pacific, suggesting a hydrothermal input. Our serpentine values (+0.13 ± 0.04 and + 0.17 ± 0.03 ‰) falls within the range of other serpentinites, whereas the aragonite vein (+0.40 ± 0.07 ‰) indicate a mixed marine seawater and hydrothermal input and a scavenging of lighter isotopes by the Mn and/or Fe rich alteration rims (Neubeck et al., 2021; Pašava et al., 2019). The tendency of Mn oxides to preferentially accumulate lighter Ni isotopes can be explained either by biological processes or by abiotic factors such as the bonding environment, zero-point energy (ZPE) or crystal field effects (Schauble, 2004). When Ni is adsorbed or incorporated, it interacts with the Mn—O framework. The vibrational frequencies in Mn oxides are determined by the Mn—O bonds in the lattice and when Ni is incorporated or adsorbed, it perturbs these vibrations and becomes part of the vibrational landscape of the oxide (Peacock and Sherman, 2007a, 2007b). The Ni—O bonds in Mn oxides are generally strong and covalent, similar to the bonding found in other oxides such as silicates and phosphates. However, despite the general principle favoring heavier isotopes in stronger bonds, the specific high-frequency vibrational environment of Mn oxides can lead to preferential incorporation of lighter Ni isotopes (Sorensen et al., 2020). This occurs because lighter isotopes, with their higher vibrational frequencies, better match the energetic landscape of the Mn oxide structure (Schauble, 2004). Thus, the Mn oxide associated with light Ni isotopes, may be explained by the high-frequency vibrational environments of the Mn oxides, which in turn will incorporate lighter isotopes. However, substitution and incorporation of metal isotopes (ZPE shifts) will lead to a lowered energy, which favor the heavier isotope, and in turn may explain the often occurring “aging” of the isotopic fractionation of laboratory synthesized minerals and the associated isotopic signature shifting from light to heavy (Little et al., 2020; Ciscato et al., 2018).

4.8. Carbon isotopes and manganese

Several studies have demonstrated that manganese oxides are commonly associated with negative carbon isotope values ranging from −11.1 to −43.8 ‰ (Neubeck et al., 2021; Zhang et al., 2024; Johnson et al., 2015). Some of these values have been interpreted as indicative of biogenic origins (Neubeck et al., 2021; Zhang et al., 2024). Johnson et al. (2015) reported on the scavenging of heavy carbon isotopes abiotically, by birnessites, suggesting that microbially formed Mn oxides might be distinguishable from abiotic ones through carbon isotope analysis. Natural Mn carbonates also typically exhibit negative carbon isotope compositions (−16.4 to +1.3 ‰), and are instead related to hydrothermal fluids with dissolved CO_2 (Starikova and Kuleshov, 2016). Most natural Mn ores show negative δ^{13}C values due to their association with the oxidation of organic matter (Kuleshov, 2003; Kuleshov et al., 2023). In contrast, the few Mn ores with slightly positive δ^{13}C values are linked to the precipitation of atmospheric CO_2 (Kuleshov et al., 2023). The preferential scavenging of carbon isotopes by Mn oxides remains largely unknown, making it challenging to interpret the biogenicity of Mn oxides based on carbon isotopes. In our samples, the serpentinite mud shows lighter carbon isotope values (−17.67 ± 0.6 ‰) compared to the mixed samples (serpentinites and dendrites, −6.75 ± 0.5 ‰), indicating an abiotic and/or mixed formation process for the dendrites. The Raman analyses did reveal carbon peaks around 1450 and 1630 cm-1, representing hydrocarbons (Romero-Sarmiento et al., 2014) and poorly ordered carbon (Beyssac et al., 2002), respectively, which is in line with previous findings of similar samples (Neubeck et al., 2021). The δ^{13}C values of −4.02 to −21 ‰, however, contrasts with an earlier study of dendrites from the same drill core but at a different depth, which reported δ^{13}C average values of −35.4 ± 0.50 ‰ for the dendrites compared to (+0.67 ± 0.40) ‰ for aragonite (Neubeck et al., 2021). The relatively narrow range of δ^{13}C values (−4.02 to −21 ‰) falls within both the abiotic and biogenic fields (Fig. 6), precluding a definitive interpretation of origin based solely on these measurements. However, in situ analyses of δ^{13}C may reveal additional trends that could aid in distinguishing between formation pathways.

5. Conclusions

This study provides new insights into the formation of three-dimensional Fe–Mn-rich dendrites, indicating a likely mixed abiotic and biotic origin for structures that extend inward from veins into serpentine muds. This mode of growth contrasts with previously reported dendrites, which developed outward into veins subsequently filled with aragonite. The dendrites documented here exhibit morphological similarities to those described in earlier studies, where Fe—Mn oxide nanoparticles are proposed to form at fluid-fluid interfaces, potentially supporting a fluid-driven formation mechanism involving viscous formation of finger-like structures.

Elemental mapping and Raman spectroscopy reveal that the dendrites are composed of disordered Fe and Mn oxides, most likely birnessite, characterized by distinctive Mn—O stretching vibrations. These structures may have formed through interactions between oxidizing,

low-viscosity fluids and more viscous serpentine muds, promoting dendritic growth in response to chemical and physical gradients or by biogenic oxidation. Notably, the presence of mature carbonaceous material within the dendrites suggests a biogenic and/or mixed origin.

Isotopic analyses, particularly δ^{60}Ni values, indicate that the Fe—Mn dendrites fractionate nickel isotopes, displaying lighter signatures relative to the surrounding serpentine and aragonite. While this pattern aligns with observations from hydrothermal, weathered ultramafic environments or black shales, it does not correspond to typical biogenic isotope signatures. In contrast, δ^{13}C values point towards a mixed abiotic–biotic origin, differing from exclusively biogenic interpretations in other parts of the drill core, which may be partly due to the mixed nature of the sample despite the micro drilling approach.

These findings underscore the complexity of Fe—Mn dendrite formation, where abiotic and biogenic processes may yield morphologically similar features with distinct geochemical characteristics. This highlights the need for more detailed microstructural and isotopic investigations to better resolve the formation mechanisms. The study further emphasizes the role of fluid dynamics and mineral precipitation in shaping the morphology and composition of Fe—Mn dendrites in serpentine-rich environments, with potential contributions from microbial activity or associated organic by-products. Taken together, the Fe—Mn dendrites presented here are likely formed through either mixed abiotic/biotic processes or reflect mixed isotopic signals, where the carbon isotopes indicate a combination of organic matter and aragonite. However, the limited sample size and the scarcity of studies on dendrites introduce uncertainty, making it difficult to draw definitive conclusions about their origin.

To advance understanding of these structures, future research should adopt a broader sampling strategy across varied geological settings, enabling more robust statistical analyses and reducing uncertainties related to the limited sample size. Expanded isotopic investigations, particularly of δ^{60}Ni and δ^{13}C values, would help refine our understanding of isotope fractionation and its relevance to distinguishing biotic, abiotic, or mixed origins. Moreover, comparisons with microstromatolites exhibiting cyclic growth laminations may aid in identifying diagnostic morphological indicators of biogenic versus abiotic processes.

CRediT authorship contribution statement

Anna Neubeck: Writing – review & editing, Writing – original draft, Validation, Project administration, Methodology, Funding acquisition, Formal analysis, Data curation, Conceptualization. **Piotr Szymczak:** Writing – review & editing, Validation, Investigation. **Vyllinniskii Cameron:** Writing – review & editing, Validation. **Daniel Buczko:** Writing – review & editing, Data curation. **Magnus Ivarsson:** Writing – review & editing.

Declaration of competing interest

The authors declare that they have no known competing financial interests or personal relationships that could have appeared to influence the work reported in this paper.

Acknowledgements

We thank Haoyi Yao at Stockholm University Stable isotope lab (SIL) for assisting with the carbon isotope analyses. This study was supported by the Swedish research council (VR) project to A.N. (#2017-05018) and the Swedish National Space board (DNR 13/100) to A.N. We also want to thank Olivier Rouxel and Malou Ollivier for help with the nickel isotope preparations and analysis. We would like to express our sincere gratitude to the reviewers for their valuable feedback, which has significantly improved the quality of the manuscript.

Appendix A. Supplementary data

Supplementary data to this article can be found online at https://doi.org/10.1016/j.chemer.2025.126303.

Data availability

The data (raw Raman data) will be made available on request. All EPMA data is presented in the manuscript.

References

Alt, J.C., Shanks III, W.C., Bach, W., Paulick, H., Garrido, C.J., Beaudoin, G., 2007. Hydrothermal alteration and microbial sulfate reduction in peridotite and gabbro exposed by detachment faulting at the mid-Atlantic ridge, 15°20′N (ODP leg 209): a sulfur and oxygen isotope study. Geochem. Geophys. Geosyst. 8. https://doi.org/10.1029/2007GC001617.

Andrews, J.E., Kendall, A.C., Hall, A., 2015. Microbial crust with Frutexites(?) and iron staining in chalks: Albian–Cenomanian boundary, Hunstanton, UK. Geol. Mag. 152, 1–11. https://doi.org/10.1017/S0016756814000107.

Archer, C., Vance, D., Milne, A., Lohan, M.C., 2020. The oceanic biogeochemistry of nickel and its isotopes: new data from the South Atlantic and the Southern Ocean biogeochemical divide. Earth Planet. Sci. Lett. 535, 116118. https://doi.org/10.1016/j.epsl.2020.116118.

Bach, W., Garrido, C.J., Paulick, H., Harvey, J., Rosner, M., 2004. Seawater-peridotite interactions: first insights from ODP leg 209, MAR 15°N. Geochem. Geophys. Geosyst. 5. https://doi.org/10.1029/2004GC000744.

Benzerara, K., Menguy, N., 2009. Looking for traces of life in minerals. Comptes Rendus Palevol, Traces de vie présente ou passé: quels indices, signatures ou marqueurs?, 8, pp. 617–628. https://doi.org/10.1016/j.crpv.2009.03.006.

Bernardini, S., Bellatreccia, F., Casanova Municchia, A., Della Ventura, G., Sodo, A., 2019. Raman spectra of natural manganese oxides. J. Raman Spectrosc. 50, 873–888. https://doi.org/10.1002/jrs.5583.

Bernardini, S., Bellatreccia, F., Della Ventura, G., Ballirano, P., Sodo, A., 2020. Raman spectroscopy and laser-induced degradation of groutellite and ramsdellite, two cathode materials of technological interest. RSC Adv. 10 (2), 923–929. https://doi.org/10.1039/c9ra08662e.

Bernardini, S., Bellatreccia, F., Columbu, A., Vaccarelli, I., Pellegrini, M., Jurado, V., Del Gallo, M., Saiz-Jimenez, C., Sodo, A., Millo, C., Jovane, L., De Waele, J., 2021a. Morpho-mineralogical and bio-geochemical description of cave manganese stromatolite-like patinas (Grotta del Cervo, Central Italy) and hints on their paleohydrological-driven genesis. Front. Earth Sci. 9. https://doi.org/10.3389/feart.2021.642667.

Bernardini, S., Bellatreccia, F., Della Ventura, G., Sodo, A., 2021b. A reliable method for determining the oxidation state of manganese at the microscale in Mn oxides via Raman spectroscopy. Geostand. Geoanal. Res. 45, 223–244. https://doi.org/10.1111/ggr.12361.

Bernardini, S., Ventura, G.D., Sodo, A., Benites, M., Jovane, L., Hein, J.R., Lucci, F., 2024. Micro-Raman mapping of critical metals (Li, Co, Ni) in a rhythmically laminated deep-ocean ferromanganese deposit. Geochemistry 84, 126014. https://doi.org/10.1016/j.chemer.2023.126014.

Bernardini, S., Ventura, G.D., Jovane, L., Sodo, A., Mihailova, B., 2025. The Stability of Manganese Oxides under Laser Irradiation during Raman Analyses: II. Layer Structures. https://analyticalsciencejournals.onlinelibrary.wiley.com/doi/10.1002/jrs.6829.

Beunon, H., Chernonozhkin, S.M., Mattielli, N., Goderis, S., Doucet, L.-S., Debaille, V., Vanhaecke, F., 2020. Innovative two-step isolation of Ni prior to stable isotope ratio measurements by MC-ICP-MS: application to igneous geological reference materials. J. Anal. At. Spectrom 35, 2213–2223. https://doi.org/10.1039/D0JA00163E.

Beyssac, O., Goffé, B., Chopin, C., Rouzaud, J.N., 2002. Raman spectra of carbonaceous material in metasediments: a new geothermometer. J. Metam. Geol. 20, 859–871. https://doi.org/10.1046/j.1525-1314.2002.00408.x.

Beyssac, O., Goffé, B., Petitet, J.-P., Froigneux, E., Moreau, M., Rouzaud, J.-N., 2003. On the characterization of disordered and heterogeneous carbonaceous materials by Raman spectroscopy. Spectrochim. Acta A Mol. Biomol. Spectrosc. 59, 2267–2276. https://doi.org/10.1016/s1386-1425(03)00070-2.

Bogoyavlenskiy, V.A., Chernova, N.A., 2000. Diffusion-limited aggregation: a relationship between surface thermodynamics and crystal morphology. Phys. Rev. E 61, 1629–1633. https://doi.org/10.1103/PhysRevE.61.1629.

Böhm, F., Brachert, T.C., 1993. Deep-water Stromatolites and Frutexites MASLOV from the Early and Middle Jurassic of S-Germany and Austria. Facies 28, 145–168.

Boskabadi, A., Pitcairn, I.K., Leybourne, M.I., Teagle, D.A.H., Cooper, M.J., Hadizadeh, H., Nasiri Bezenjani, R., Monazzami Bagherzadeh, R., 2020. Carbonation of ophiolitic ultramafic rocks: listvenite formation in the late cretaceous ophiolites of eastern Iran. Lithos 352-353, 105307. https://doi.org/10.1016/j.lithos.2019.105307.

Buckman, S., Ashley, P., 2010. Silica-carbonate (listwanites) related gold mineralisation associated with epithermal alteration of serpentinite bodies.

Cameron, V., Vance, D., 2014. Heavy nickel isotope compositions in rivers and the oceans. Geochim. Cosmochim. Acta 128, 195–211. https://doi.org/10.1016/j.gca.2013.12.007.

Cameron, V., Vance, D., Archer, C., House, C.H., 2009. A biomarker based on the stable isotopes of nickel. Proc. Natl. Acad. Sci. 106, 10944–10948. https://doi.org/10.1073/pnas.0900726106.

Cavalazzi, B., Barbieri, R., Ori, G.G., 2007. Chemosynthetic microbialites in the Devonian carbonate mounds of Hamar Laghdad (Anti-Atlas, Morocco). Sediment. Geol. 200, 73–88. https://doi.org/10.1016/j.sedgeo.2007.03.002.

Chen, L.-M., Lightfoot, P.C., Zhu, J.-M., Teng, F.-Z., Duan, Q., Yin, R., Wu, G., Yu, S.-Y., Hu, R.-Z., 2023. Nickel isotope ratios trace the process of sulfide-silicate liquid immiscibility during magmatic differentiation. Geochim. Cosmochim. Acta 353, 1–12. https://doi.org/10.1016/j.gca.2023.05.013.

Chernonozhkin, S.M., Goderis, S., Lobo, L., Claeys, P., Vanhaecke, F., 2015. Development of an isolation procedure and MC-ICP-MS measurement protocol for the study of stable isotope ratio variations of nickel. J. Anal. At. Spectrom 30, 1518–1530. https://doi.org/10.1039/C5JA00080G.

Chernyshova, I., Hochella, M., Elwood Madden, A., 2007. Size-dependent structural transformations of hematite nanoparticles. 1. Phase transition. Phys. Chem. Chem. Phys. 9, 1736–1750. https://doi.org/10.1039/b618790k.

Chopard, B., Herrmann, H.J., Vicsek, T., 1991. Structure and growth mechanism of mineral dendrites. Nature 353, 409–412. https://doi.org/10.1038/353409a0.

Ciscato, E.R., Bontognali, T.R.R., Vance, D., 2018. Nickel and its isotopes in organic-rich sediments: implications for oceanic budgets and a potential record of ancient seawater. Earth Planet. Sci. Lett. 494, 239–250. https://doi.org/10.1016/j.epsl.2018.04.061.

Dong, Z.-G., Peng, Z.-D., Robbins, L.J., Konhauser, K.O., Zhang, B.-L., Zhang, L.-C., Li, J., Li, W.-J., Zhang, L., Wang, C.-L., 2023. Episodic ventilation of euxinic bottom waters triggers the formation of black shale-hosted Mn carbonate deposits. Geochim. Cosmochim. Acta 341, 132–149. https://doi.org/10.1016/j.gca.2022.11.027.

Dupraz, C., Reid, R., Braissant, O., Decho, A., Norman, R., Visscher, P., 2009. Processes of carbonate precipitation in modern microbial mats. Earth Sci. Rev. 96, 141–162. https://doi.org/10.1016/j.earscirev.2008.10.005.

Eder, V.G., Föllmi, K.B., Zanin, Y.N., Zamirailova, A.G., 2018. Manganese carbonates in the Upper Jurassic Georgiev Formation of the Western Siberian marine basin. Sedimentary Geology 363, 221–234. https://doi.org/10.1016/j.sedgeo.2017.11.012.

Eshraghi, M., Hashemi, M., Jelinek, B., Felicelli, S.D., 2017. Three-dimensional lattice Boltzmann modeling of dendritic solidification under forced and natural convection. Metals 7 (11), 474.

Fleischmann, S., Du, J., Chatterjee, A., McManus, J., Iyer, S.D., Amonkar, A., Vance, D., 2023. The nickel output to abyssal pelagic manganese oxides: a balanced elemental and isotope budget for the oceans. Earth Planet. Sci. Lett. 619, 118301. https://doi.org/10.1016/j.epsl.2023.118301.

Fujii, T., Moynier, F., Dauphas, N., Abe, M., 2011. Theoretical and experimental investigation of nickel isotopic fractionation in species relevant to modern and ancient oceans. Geochim. Cosmochim. Acta 75, 469–482. https://doi.org/10.1016/j.gca.2010.11.003.

Gall, L., Williams, H., Siebert, C., Halliday, A., 2012. Determination of mass-dependent variations in nickel isotope compositions using double spiking and MC-ICPMS. J. Anal. At. Spectrom 27, 137–145. https://doi.org/10.1039/C1JA10209E.

Gall, L., Williams, H.M., Siebert, C., Halliday, A.N., Herrington, R.J., Hein, J.R., 2013. Nickel isotopic compositions of ferromanganese crusts and the constancy of deep ocean inputs and continental weathering effects over the Cenozoic. Earth Planet. Sci. Lett. 375, 148–155. https://doi.org/10.1016/j.epsl.2013.05.019.

Gall, L., Williams, H.M., Halliday, A.N., Kerr, A.C., 2017. Nickel isotopic composition of the mantle. Geochim. Cosmochim. Acta 199, 196–209.

Garcia-Ruiz, J., Otálora, F., Sanchez-Navas, A., Higes-Rolando, F., 1994. The formation of manganese dendrites as the mineral record of flow structures, pp. 307–318. https://doi.org/10.1007/978-3-662-07304-9_23.

Green-Pedersen, H., Jensen, B.T., Pind, N., 1997. Nickel adsorption on MnO2, Fe(OH)3, montmorillonite, humic acid and calcite: a comparative study. Environ. Technol. 18, 807–815. https://doi.org/10.1080/09593331808616599.

Gueguen, B., Rouxel, O., 2021. The nickel isotope composition of the authigenic sink and the diagenetic flux in modern oceans. Chem. Geol. 563, 120050. https://doi.org/10.1016/j.chemgeo.2020.120050.

Gueguen, B., Rouxel, O., Ponzevera, E., Bekker, A., Fouquet, Y., 2013. Nickel isotope variations in terrestrial silicate rocks and geological reference materials measured by MC-ICP-MS. Geostand. Geoanalytical Res. 37, 297–317. https://doi.org/10.1111/j.1751-908X.2013.00209.x.

Gueguen, B., Rouxel, O., Rouget, M.-L., Bollinger, C., Ponzevera, E., Germain, Y., Fouquet, Y., 2016. Comparative geochemistry of four ferromanganese crusts from the Pacific Ocean and significance for the use of Ni isotopes as paleoceanographic tracers. Geochim. Cosmochim. Acta 189, 214–235. https://doi.org/10.1016/j.gca.2016.06.005.

Gueguen, B., Rouxel, O., Fouquet, Y., 2021. Nickel isotopes and rare earth elements systematics in marine hydrogenetic and hydrothermal ferromanganese deposits. Chem. Geol. 560, 119999. https://doi.org/10.1016/j.chemgeo.2020.119999.

Heim, C., Quéric, N.-V., Ionescu, D., Schäfer, N., Reitner, J., 2017. Frutexites-like structures formed by iron oxidizing biofilms in the continental subsurface (Äspö Hard Rock Laboratory, Sweden). PloS One 12, e0177542. https://doi.org/10.1371/journal.pone.0177542.

Hein, J.R., Mizell, K., Koschinsky, A., Conrad, T.A., 2013. Deep-ocean mineral deposits as a source of critical metals for high- and green-technology applications: comparison with land-based resources. Ore Geol. Rev. 51, 1–14. https://doi.org/10.1016/j.oregeorev.2012.12.001.

Hiebert, R.S., Bekker, A., Houlé, M.G., Rouxel, O.J., 2022. Nickel isotope fractionation in komatiites and associated sulfides in the Hart deposit, late Archean Abitibi Greenstone Belt, Canada. Chem. Geol. 603, 120912. https://doi.org/10.1016/j.chemgeo.2022.120912.

Hou, Z., Woś, D., Tschegg, C., Rogowitz, A., Rice, A.H.N., Nasdala, L., Fusseis, F., Szymczak, P., Grasemann, B., 2023. Three-dimensional mineral dendrites reveal a nonclassical crystallization pathway. Geology 51, 626–630. https://doi.org/10.1130/G51127.1.

Huang, M., Li, F., Dong, F., Zhang, Y.X., Zhang, L.L., 2015. MnO2-based nanostructures for high-performance supercapacitors. J. Mater. Chem. A 3, 21380–21423. https://doi.org/10.1039/C5TA05523G.

Huld, S., McMahon, S., Sjöberg, S., Huang, P., Neubeck, A., 2023. Chemical gardens mimic electron paramagnetic resonance spectra and morphology of biogenic Mn oxides. Astrobiology 23, 24–32. https://doi.org/10.1089/ast.2021.0194.

Ivarsson, M., 2006. Advantages of doubly polished thin sections for the study of microfossils in volcanic rock. Geochem. Trans. 7, 5. https://doi.org/10.1186/1467-4866-7-5.

Ivarsson, M., Bach, W., Broman, C., Neubeck, A., Bengtson, S., 2018. Fossilized life in subseafloor ultramafic rocks. New York: Taylor & Francis Ltd Geomicrobiology 35 (6), 460–467.

Jeong, J.-H., Goldenfeld, N., Dantzig, J.A., 2001. Phase field model for three-dimensional dendritic growth with fluid flow. Phys. Rev. E 64, 041602.

Johnson, K., Purvis, G., Lopez-Capel, E., Peacock, C., Gray, N., Wagner, T., März, C., Bowen, L., Ojeda, J., Finlay, N., Robertson, S., Worrall, F., Greenwell, C., 2015. Towards a mechanistic understanding of carbon stabilization in manganese oxides. Nat. Commun. 6, 7628. https://doi.org/10.1038/ncomms8628.

Jung, H., 2017. Abiotic- and biotic-formation of manganese oxides and their fate in environmental systems (dissertation). Washington University, St. Louis.

Junta, J.L., Hochella, M.F., 1994. Manganese (II) oxidation at mineral surfaces: a microscopic and spectroscopic study. Geochim. Cosmochim. Acta 58, 4985–4999. https://doi.org/10.1016/0016-7037(94)90226-7.

Kazmierczak, J., Kempe, S., 2006. Genuine modern analogues of Precambrian stromatolites from caldera lakes of Niuafo'ou Island, Tonga. Naturwissenschaften 93, 119–126. https://doi.org/10.1007/s00114-005-0066-x.

Kelemen, P.B., Kikawa, E., Miller, D.J., et al., 2004. Proc. ODP, Init. Repts., 209: College Station, TX (Ocean Drilling Program). https://doi.org/10.2973/odp.proc.ir.209.2004Link. http://www-odp.tamu.edu/publications/citations/cite209.html.

Klaver, M., Ionov, D.A., Takazawa, E., Elliott, T., 2020. The non-chondritic Ni isotope composition of earth's mantle. Geochim. Cosmochim. Acta 268, 405–421. https://doi.org/10.1016/j.gca.2019.10.017.

Kuleshov, V.N., 2003. Isotopic composition (δ13C, δ18O) and origin of manganese carbonate ores from the early oligocene deposits, the eastern Paratethys. Geochemistry 63, 329–363. https://doi.org/10.1078/0009-2819-00029.

Kuleshov, V.N., Bychkov, A.Yu., Nikolaeva, I.Yu., Tarnopolskaya, M.E., 2023. Rare earth elements (REE) and isotope composition (δ13C and δ18O) of manganese ores of Chiatura deposit (Georgia): features of ore formation and genesis. Acta Geochim. 42, 779–801. https://doi.org/10.1007/s11631-023-00614-w.

Lemaitre, N., Du, J., de Souza, G.F., Archer, C., Vance, D., 2022. The essential bioactive role of nickel in the oceans: evidence from nickel isotopes. Earth Planet. Sci. Lett. 584, 117513. https://doi.org/10.1016/j.epsl.2022.117513.

Li, D., Yang, J., Tang, W., Wu, X., Wei, L., Chen, Y., 2014. Controlled synthesis of hierarchical MnO2 microspheres with hollow interiors for the removal of benzene. RSC Adv. 4, 26796–26803. https://doi.org/10.1039/C4RA01146E.

Li, M., Grasby, S.E., Wang, S.-J., Zhang, X., Wasylenki, L.E., Xu, Y., Sun, M., Beauchamp, B., Hu, D., Shen, Y., 2021. Nickel isotopes link Siberian traps aerosol particles to the end-Permian mass extinction. Nat. Commun. 12, 2024. https://doi.org/10.1038/s41467-021-22066-7.

Li, F., Yin, H., Zhu, T., Zhuang, W., 2024. Understanding the role of manganese oxides in retaining harmful metals: insights into oxidation and adsorption mechanisms at microstructure level. Eco-Environ. Health 3, 89–106.

Little, S.H., Archer, C., McManus, J., Najorka, J., Wegorzewski, A.V., Vance, D., 2020. Towards balancing the oceanic Ni budget. Earth Planet. Sci. Lett. 547, 116461. https://doi.org/10.1016/j.epsl.2020.116461.

Liu, C., Calo, V.M., Regenauer-Lieb, K., Hu, M., 2023. Dendritic growth patterns in rocks: inverting the driving and triggering mechanisms. J. Geophys. Res. Solid Earth 128, e2023JB027105. https://doi.org/10.1029/2023JB027105.

Madden, A.S., Hochella, M.F., 2005. A test of geochemical reactivity as a function of mineral size: manganese oxidation promoted by hematite nanoparticles. Geochim. Cosmochim. Acta 69, 389–398. https://doi.org/10.1016/j.gca.2004.06.035.

McLoughlin, N., Brasier, M.D., Wacey, D., Green, O.R., Perry, R.S., 2007. On biogenicity criteria for endolithic microborings on early earth and beyond. Astrobiology 7, 10–26. https://doi.org/10.1089/ast.2006.0122.

Moynier, F., Blichert-Toft, J., Telouk, P., Luck, J.-M., Albarede, F., 2007. Comparative stable isotope geochemistry of Ni, Cu, Zn, and Fe in chondrites and iron meteorites. Geochim. Cosmochim. Acta 71, 4365–4379. https://doi.org/10.1016/j.gca.2007.06.049.

Myrow, P.M., Coniglio, M., 1991. Origin and diagenesis of Cryptobiontic Frutexites in the Chapel Island formation (Vendian to early Cambrian) of Southeast Newfoundland, Canada. PALAIOS 6, 572–585. https://doi.org/10.2307/3514920.

Neubeck, A., Ivarsson, M., Broman, C., Lima-Zaloumis, J., Bach, W., Whitehouse, M., 2021. Carbon isotopic composition of Frutexites in subseafloor ultramafic rocks. Biogeochemistry 154, 525–536. https://doi.org/10.1007/s10533-021-00806-7.

Oaki, Y., Imai, H., 2003. Experimental demonstration for the morphological evolution of crystals grown in gel media. Cryst. Growth Des. 3, 711–716. https://doi.org/10.1021/cg034053e.

Ostrooumov, M., 2017. Raman and infrared reflection spectroscopic study of mineralogical composition of iron-manganese nodules (Pacific and Indian oceans). Int J Exp Spectroscopic Tech 2, 012.

Pašava, J., Chrastný, V., Loukola-Ruskeeniemi, K., Šebek, O., 2019. Nickel isotopic variation in black shales from Bohemia, China, Canada, and Finland: a reconnaissance study. Miner. Deposita 54, 719–742. https://doi.org/10.1007/s00126-018-0839-8.

Peacock, C.L., Sherman, D.M., 2007a. Crystal-chemistry of Ni in marine ferromanganese crusts and nodules. Am. Mineral. 92, 1087–1092. https://doi.org/10.2138/am.2007.2378.

Peacock, C.L., Sherman, D.M., 2007b. Sorption of Ni by birnessite: equilibrium controls on Ni in seawater. Chem. Geol. 238, 94–106.

Pearson, R.G., 1963. Hard and soft acids and bases | journal of the American Chemical Society. J. Am. Chem. Soc. 85.

Pyle, G., Couture, P., 2011. 5 - Nickel. In: Wood, C.M., Farrell, A.P., Brauner, C.J. (Eds.), Fish physiology, homeostasis and toxicology of essential metals. Academic Press, pp. 253–289. https://doi.org/10.1016/S1546-5098(11)31005-9.

Ragsdale, S.W., 2007. Nickel and the carbon cycle. In: J. Inorg. Biochem., Special Issue in Memory of Edward I. Stiefel, 101, pp. 1657–1666. https://doi.org/10.1016/j.jinorgbio.2007.07.014.

Ragsdale, S.W., 2009. Nickel-based enzyme systems*. J. Biol. Chem. 284, 18571–18575. https://doi.org/10.1074/jbc.R900020200.

Ratié, G., Jouvin, D., Garnier, J., Rouxel, O., Miska, S., Guimarães, E., Vieira, L.C., Sivry, Y., Zelano, I., Montarges-Pelletier, E., Thil, F., Quantin, C., 2015. Nickel isotope fractionation during tropical weathering of ultramafic rocks. Chem. Geol. 402, 68–76. https://doi.org/10.1016/j.chemgeo.2015.02.039.

Ratnayake, D.M., Tanaka, R., Nakamura, E., 2021. Novel nickel isolation procedure for a wide range of sample matrices without using dimethylglyoxime for isotope measurements using MC-ICP-MS. Anal. Chim. Acta 1181, 338934. https://doi.org/10.1016/j.aca.2021.338934.

Romero-Sarmiento, M.-F., Rouzaud, J.-N., Bernard, S., Deldicque, D., Thomas, M., Littke, R., 2014. Evolution of Barnett Shale organic carbon structure and nanostructure with increasing maturation. Org. Geochem. 71, 7–16. https://doi.org/10.1016/j.orggeochem.2014.03.008.

Saenko, E., 2024. Doping birnessite as a method for synthesizing an ion exchanger selective to strontium and repeatedly working in sorption-desorption cycles. J. Solid State Chem. Volume 329, 124381. ISSN 0022-4596. https://doi.org/10.1016/j.jssc.2023.124381.

Saito, Y., Ueta, T., 1989. Monte Carlo studies of equilibrium and growth shapes of a crystal. Phys. Rev. A 40, 3408–3419. https://doi.org/10.1103/PhysRevA.40.3408.

Saunders, J.A., 2022. Colloids and nanoparticles: implications for hydrothermal precious metal ore formation. SEG Discovery 15–21. https://doi.org/10.5382/SEGnews.2022-130.fea-01.

Saunders, J.A., Schoenly, P.A., 1995. Boiling, colloid nucleation and aggregation, and the genesis of bonanza Au-Ag ores of the sleeper deposit. Nevada. Mineral. Deposita 30, 199–210. https://doi.org/10.1007/BF00196356.

Schauble, E.A., 2004. Applying stable isotope fractionation theory to new systems. Rev. Mineral. Geochem. 55, 65–111. https://doi.org/10.2138/gsrmg.55.1.65.

Schoenly, P.A., Saunders, J.A., 1993. NATURAL GOLD DENDRITES FROM HYDROTHERMAL Au-Ag DEPOSITS: CHARACTERISTICS AND COMPUTER SIMULATIONS. Fractals 01, 585–593. https://doi.org/10.1142/S0218348X93000617.

Sjöberg, S., Yu, C., Stairs, C.W., Allard, B., Hallberg, R., Henriksson, S., Åström, M., Dupraz, C., 2021. Microbe-mediated Mn oxidation—a proposed model of mineral formation. Minerals 11, 1146. https://doi.org/10.3390/min11101146.

Sorensen, J.V., Gueguen, B., Stewart, B.D., Peña, J., Rouxel, O., Toner, B.M., 2020. Large nickel isotope fractionation caused by surface complexation reactions with hexagonal birnessite. Chem. Geol. 537, 119481. https://doi.org/10.1016/j.chemgeo.2020.119481.

Spivak-Birndorf, L.J., Wang, S.-J., Bish, D.L., Wasylenki, L.E., 2018. Nickel isotope fractionation during continental weathering. Chem. Geol. 476, 316–326. https://doi.org/10.1016/j.chemgeo.2017.11.028.

Starikova, E.V., Kuleshov, V.N., 2016. Isotopic composition (δ13C and δ18O) and genesis of carbonates from the famennian manganiferous formation of Pai-Khoi. Lithol. Miner. Resour. 51, 195–213. https://doi.org/10.1134/S0024490216030068.

Steele, R.C.J., Elliott, T., Coath, C.D., Regelous, M., 2011. Confirmation of mass-independent Ni isotopic variability in iron meteorites. Geochim. Cosmochim. Acta 75, 7906–7925. https://doi.org/10.1016/j.gca.2011.08.030.

Suekane, T., Ono, J., Hyodo, A., Nagatsu, Y., 2017. Three-dimensional viscous fingering of miscible fluids in porous media. Phys. Rev. Fluids 2, 103902. https://doi.org/10.1103/PhysRevFluids.2.103902.

Suekane, T., Koe, T., Barbancho, P.M., 2019. Three-dimensional interaction of viscous fingering and gravitational segregation in porous media. Fluids 4, 130. https://doi.org/10.3390/fluids4030130.

Sutherland, K.M., Wankel, S.D., Hein, J.R., Hansel, C.M., 2020. Spectroscopic insights into ferromanganese crust formation and diagenesis. Geochem. Geophys. Geosyst. 21, e2020GC009074. https://doi.org/10.1029/2020GC009074.

Takano, S., Tanimizu, M., Hirata, T., Shin, K.-C., Fukami, Y., Suzuki, K., Sohrin, Y., 2017. A simple and rapid method for isotopic analysis of nickel, copper, and zinc in seawater using chelating extraction and anion exchange. Anal. Chim. Acta 967, 1–11. https://doi.org/10.1016/j.aca.2017.03.010.

Tebo, B.M., Bargar, J.R., Clement, B.G., Dick, G.J., Murray, K.J., Parker, D., Verity, R., Webb, S.M., 2004. BIOGENIC MANGANESE OXIDES: properties and mechanisms of formation. Annu. Rev. Earth Planet. Sci. 32, 287–328. https://doi.org/10.1146/annurev.earth.32.101802.120213.

Vance, D., Little, S.H., Archer, C., Cameron, V., Andersen, M.B., Rijkenberg, M.J.A., Lyons, T.W., 2016. The oceanic budgets of nickel and zinc isotopes: the importance of sulfidic environments as illustrated by the Black Sea. Philos. Trans. R. Soc. Math. Phys. Eng. Sci. 374, 20150294. https://doi.org/10.1098/rsta.2015.0294.

Wagner, T., Magill, C.R., Herrle, J.O., 2018. Carbon isotopes. In: White, W.M. (Ed.), Encyclopedia of Geochemistry: A Comprehensive Reference Source on the Chemistry of the Earth. Springer International Publishing, Cham, pp. 194–204. https://doi.org/10.1007/978-3-319-39312-4_176.

Walter, M.R., Awramik, S.M., 1979. Frutexites from stromatolites of the Gunflint Iron Formation of Canada, and its biological affinities. Precambrian Res. 9, 23–33. https://doi.org/10.1016/0301-9268(79)90049-4.

Wang, X., Lan, S., Zhu, M., Ginder-Vogel, M., Yin, H., Liu, F., Tan, W., Feng, X., 2015. The presence of ferrihydrite promotes abiotic formation of manganese (Oxyhydr)oxides. Soil Sci. Soc. Am. J. 79, 1297–1305. https://doi.org/10.2136/sssaj2014.12.0502.

Wang, S.-J., Wang, W., Zhu, J.-M., Wu, Z., Liu, J., Han, G., Teng, F.-Z., Huang, S., Wu, H., Wang, Y., Wu, G., Li, W., 2021. Nickel isotopic evidence for late-stage accretion of mercury-like differentiated planetary embryos. Nat. Commun. 12, 294. https://doi.org/10.1038/s41467-020-20525-1.

Wasylenki, L.E., Wells, R.M., Spivak-Birndorf, L.J., 2014. Ni sorption to birnessite drives a surprisingly large fractionation 2014, EP23D-3623.

Wasylenki, L.E., Wells, R.M., Spivak-Birndorf, L.J., Baransky, E.J., Frierdich, A.J., 2024. Toward mending the marine mass balance model for nickel: experimentally determined isotope fractionation during Ni sorption to birnessite. Geochim. Cosmochim. Acta 379, 76–88. https://doi.org/10.1016/j.gca.2024.06.022.

Xu, H., Peng, X., Ta, K., Liu, S., 2024. Fluid-related manganese deposits at the incoming plate of the Southern Mariana subduction zone. Chem. Geol. 663, 122294. https://doi.org/10.1016/j.chemgeo.2024.122294.

Zhang, Y., Li, J., Chen, L., Wei, Y., Shi, Q., Wang, D.-G., Wu, Q.-M., Song, L.-Y., Tian, M., Kuang, H.-W., Liu, Y.-Q., Mänd, K., Bai, H.-Q., Liu, Z.-L., Wang, Y.-C., Qiao, D.-W., Zhu, W.-J., 2021. Manganese carbonate stromatolites of the Ediacaran Doushantuo formation in Chengkou, northern Yangtze craton, China. J. Palaeogeogr. 10, 22. https://doi.org/10.1186/s42501-021-00099-9.

Zhang, B., Cao, J., Hu, K., Liao, Z., Zhang, R., Zhang, Y., Shi, C., Konhauser, K.O., 2024. A new negative carbon isotope interval caused by manganese redox cycling after the Shuram excursion. J. Geophys. Res. Solid Earth 129, e2023JB028307. https://doi.org/10.1029/2023JB028307.

Zwicker, J., Smrzka, D., Gothieu, M., Libowitzky, E., Joachimski, M.M., Böttcher, M.E., Peckmann, J., 2023. Chemotrophy-based phosphatic microstromatolites from the Mississippian at Drewer, Rhenish Massif, Germany. Geol. Mag. 160, 1446–1462. https://doi.org/10.1017/S0016756823000493.